AIAA 2005-3542

The Compressible Taylor-Culick Flow

Joseph Majdalani
Advanced Theoretical Research Center
University of Tennessee Space Institute
Tullahoma, TN 37388

41st AIAA/ASME/SAE/ASEE Joint Propulsion Conference and Exhibit
10–13 July 2005
Tucson, AZ

41st AIAA/ASME/SAE/ASEE Joint Propulsion Conference and Exhibit
10-13 July 2005, Tucson, Arizona

AIAA 2005-3542

The Compressible Taylor-Culick Flow

Joseph Majdalani*
University of Tennessee Space Institute, Tullahoma, TN 37388

We consider the compressible flow analogue of the well-known Taylor-Culick profile. We first present the compressible Euler equations for steady, axisymmetric, isentropic flow assuming uniform injection of a calorically perfect gas in a porous chamber. We then apply a Rayleigh-Janzen expansion in powers of M_w^2, where M_w is the wall Mach number. We solve the ensuing equations to order M_w^4 and apply the results up to the sonic point in a nozzleless chamber. Area-averaging is also performed to reconcile with one-dimensional theory. Our groundbreaking solution agrees with existing theory to the extent that it faithfully captures the steepening of the Taylor-Culick profile with downstream movement. Based on the closed-form expressions that we obtain, the main flow attributes are quantified parametrically and compared to existing incompressible and quasi-one-dimensional theories. Verification by computational fluid dynamics is also undertaken. Comparison with two turbulent flow models shows excellent agreement, particularly, in retracing the streamwise evolution of the velocity. Regardless of the Mach number, we observe nearly identical trends in chambers that are rescaled by the (critical) sonic length, L_s. Using a suitable transformation, we prove the attendant similarity and provide universal criteria that can be used to assess the relative importance of gas compression in solid and hybrid rockets. Due to sharper velocity gradients at the wall, we find that an incompressible model underestimates the skin friction along the wall and underpredicts the centerline speed by as much as 13% at the sonic point. In practice, such deviations become appreciable for large injection rates or chamber aspect ratios.

Nomenclature

a	=	chamber radius
a_0	=	sonic speed at chamber origin, $a_0 = \sqrt{\gamma p_0 / \rho_0}$
p	=	pressure normalized by headwall condition, $\overline{p} / p_0$
r , z	=	normalized radial and streamwise coordinates, $\overline{r} / a$, $\overline{z} / a$
$\boldsymbol{u}$	=	normalized velocity $(\overline{u}_r , \overline{u}_z) / a_0$
U_0 , u_0	=	centerline speed at headwall, $\overline{u}_z(0,0)$, U_0 / U_w
u_h	=	headwall injection constant, $u_0 / \pi = U_0 / (\pi U_w)$
U_w	=	wall injection velocity, $-\overline{u}_r(a, \overline{z})$
α, β, σ	=	pure constants
μ , ρ	=	dynamic viscosity and density, μ, ρ
η	=	recurring group variable, $\frac{1}{2}\pi^2 r^2$
δ, λ	=	functions of γ defined via Eqs. (68)–(69)

Subscripts and Symbols

c , s	=	centerline or sonic condition
h	=	headwall condition in the gas
m	=	area-averaged mean value
$\underline{w}$	=	sidewall condition in the gas
$\sim$,	=	dimensional or approximate variable

*Jack D. Whitfield Professor of High Speed Flows, Department of Mechanical, Aerospace and Biomedical Engineering. Member AIAA.

I. Introduction

THE injection-driven flow of an incompressible fluid was first described by Taylor[1] who not only resolved this problem in porous tubes, but also, in channels, wedges, and cones. In lieu of using Taylor's integral equation, other investigators, such as Yuan,[2] Yuan and Finkelstein,[3] Wageman and Guevara,[4] Terrill,[5,6] and Culick[7] used different routes and recovered, in the inviscid limit, the same cosine-shaped profile found by Taylor. Some of these studies relied on the vorticity-streamfunction approach or asymptotic tools to perturb the similarity-reduced equation derived by Berman[8] for steady laminar flow in porous channels.

In addition to its sheer simplicity, the Taylor-Culick solution would later prove surprisingly accurate in modeling the drainage of watery suspensions across porous sheets, in surface ablation and sweat cooling (Yuan,[9] and Peng and Yuan[10]), and in simulating the mean flow in solid rocket motors (SRMs). This could be attributed, in part, to its streamlines being observant of the no slip requirement at the sidewall, a feature that has inspired a few to coin it 'quasi-viscous.' It quickly resembled the viscous solution with successive increases in the injection Reynolds number.

Following the inventive experiments by Taylor[1] under laminar conditions, Wageman and Guevara,[4] and Yamada, Goto and Ishikawa[11] confirmed the same behavior under Reynolds numbers that were sufficiently high to induce turbulence. Turbulence appeared to have little bearing on altering the mean flow structure except in the downstream segment of the chamber where flow steepening was observed. In this part of the domain, compressibility intensified to the extent that it became difficult to discern which of the two mechanisms was more responsible for the steepening effect. The flattened shape was further reported in cold-flow experiments by Dunlap, Willoughby and Hermsen[12] and Traineau, Hervat and Kuentzmann;[13] these employed Nitrogen and air injection, respectively. The spatial evolution was also parametrically substantiated via numerical simulations by Beddini,[14] Baum, Levine and Lovine,[15] Sabnis, Gibeling and McDonald,[16] Liou and Lien,[17] and Apte and Yang.[18,19] In summary, these studies confirmed the existence of a laminar segment that could stretch over the entire length of the chamber depending on the injection Reynolds number. They also suggested that, in sufficiently long chambers, transition from the classic solution typically occurred past the midsection plane, although transition of the mean velocity was delayed to the fully developed section where the axial profile became fuller. Both compressibility and turbulence were posited as plausible candidates for causing these departures.

The ability of the Taylor-Culick equation to faithfully imitate the motion of reactive gases ejected from the regressing wall of a solid propellant rocket has vast implications and, as such, has been the subject of much scrutiny. In one study, Majdalani, Vyas and Flandro[20] have shown that, unless the burning rate is exceedingly high, the slow expansion of the sidewall may be discounted in favor of a quasi-steady model. Moreover, the idea of a uniform burning rate along the grain and the attendant assumption of constant mass addition at the sidewall have been reiterated in both nozzle-adapted and nozzleless configurations. In the latter case, Gany and Aharon[21] have pointed out that the axially accentuated erosive-burning effects on the regression rate are generally offset by the decreasing pressure in the downstream direction. In the same vein, the nearly non-reactive environment outside of the thin propellant flame zone has been repeatedly simulated and shown to be appropriately treatable by cold-flow models (see Chu, Yang and Majdalani[22]). This can be ascribed to the weak coupling with the energy equation where the temperature is almost uniform (see Vuillot[23]). Such factors have placed Taylor's mean flow formula at the epicenter of a large body of theoretical investigations focused on modeling rocket performance, flame zone analysis, particle-mean flow interactions, and the ever-daunting task of predicting aeroacoustic instability. Relevance to internal ballistics and performance prediction in rockets is briefly outlined by Majdalani.[24] By way of example, the accuracy of Taylor's formula has given Varapaev and Yagodkin[25] the impetus to use it at the basis of their investigation of hydrodynamic instability. In the same context, it has been employed by Griffond, Casalis and Pineau[26] to investigate the evolution of turbulence in straight porous cylinders. It has been essential to the evaluation of particle-mean flow interactions as demonstrated by Féraille and Casalis.[27]

The need for refined analytical solutions has since continued to grow hand-in-hand with computer muscle for two fundamental reasons. First, to gain deeper physical insight into an 'eternally complex problem,' and, second, to provide the much needed limiting process validations for numerical simulations of chemically reactive rocket chambers. As argued by Wasistho, Balachandar and Moser,[28] a team of researchers at the University of Illinois' Center for Simulation of Advanced Rockets (CSAR) has determined that analytical models often present the only valuable resource for checking numerical results; this is partly caused by the difficulty in acquiring specific experimental data and, partly, due to the harsh environment erupting in rocket chambers, particularly, one that is hostile to proper instrumentation. In the same study, Wasistho and coworkers have suggested the need to employ a compressible mean flow model to promote better agreement with their full-scale computations. Their steady and

unsteady flow results were compared, respectively, to the numerical solution of the integral equation obtained by Balakrishnan, Liñan and Williams,[29] and to the time-dependent expression for wave motion by Majdalani and Flandro.[30] Favorable agreement was noted on both counts. Today, as regulatory requirements for validation and verification continue to mount in the propulsion industry, so are the demands for improved analytical tools. In this study, we focus on the compressible Taylor flow analogue.

The quest for a compressible mean flow expression serves multiple objectives. First, it is needed to ameliorate our representation of the undisturbed inviscid field and its impact on the ensuing acoustic wave motion and flame zone analysis. For instance, it will help to obtain a more consistent solution for the total internal flowfield by insisting that both mean and unsteady components retain a compressible ingredient. Existing expressions for the time-dependent flowfield are based on an incompressible steady flow representation in both planar and axisymmetric chambers (cf. Majdalani and Roh,[31] Majdalani,[32] and Majdalani and Flandro.[30]) By the same token, a compressible outer solution can be indispensable in analyzing the thin flame zone that forms above the surface of a solid propellant or a hybrid fuel where pyrolysis and vaporization must be carefully modeled. It has often been reported that the exothermic viscous layer treatment cannot be completed without a compressible outer approximation (see Balakrishnan, Liñan and Williams[33]). Second, it is to upgrade our analysis of hydrodynamic instability which so far has been limited to incompressible equations. The use of a compressible formula at the baseline of such development can markedly improve the actual methodology and its potential outcome. Venugopal[34] shows that a minor increase in mean flow velocity caused by density variations along the wall can engender large excursions in the growth of disturbances in a simulated SRM. Third, it is to provide a more precise platform for calculating the acoustic growth rate factors inherited from volume integrals of internal flow components (Flandro[35] and Flandro and Majdalani[36]). Fourth, it is to facilitate the characterization of nozzleless rocket motors whose increased volumetric efficiency has made them prime candidates for ramjet-boosting applications. The absence of a nozzle has enabled investigators to focus on specific features of the flow, thus providing an attractive vehicle for academic studies that employ either experimentation or computation. The operation of such motors has been examined from one- and two-dimensional perspectives by Traineau, Hervat and Kuentzmann,[13] Gany and Aharon,[37] and King.[21] It has been recently considered by Balakrishnan, Liñan and Williams[29] who followed Traineau and coworkers in presenting an inviscid, rotational, and compressible integral equation that can be solved numerically in two dimensions. Using scaling arguments, their radial momentum equation was discarded and a perturbation expansion was implemented using the reciprocal of the aspect ratio. In the process, pressure and grain regression were related by the Saint-Robert power law. The resulting 'pseudo-two-dimensional' approximation has proven adequate in treating long motors with arbitrary cross-section and wall injection rate.

In this study, we reconsider Taylor's original problem in an axisymmetric, constant-area chamber with uniform wall injection. We also permit the imposition of sinusoidal injection at the headwall. Using a Rayleigh-Janzen expansion in the wall Mach number, we expand the system of equations up to fourth order and extract the compressible flow analogue of Taylor's solution.

II. Mathematical Model

A. Geometry

We consider the steady, inviscid and non-heat conducting flow of an ideal gas in the domain bounded by the porous sidewall of a tube of radius a and finite length L_0. We assume that the speed of the gas at the wall U_w is uniform and that L_0 can reach the sonic length. In solid and hybrid rockets, the sidewall velocity $U_w = \rho_P \dot{r}_P / \rho$ is commensurate with the solid or fuel propellant regression rate, $\dot{r}_P$. To justify a constant U_w, we recall that the streamwise depreciation in pressure and its wall-coupling effect can nearly offset the axial decrease in density. As shown in Fig. 1, $\bar{r}$ and $\bar{z}$ stand for the radial and streamwise coordinates (with the overbar denoting a dimensional quantity). We normalize these variables by a and select a curvilinear coordinate system whose origin is centered at the headwall. Axial symmetry reduces the field investigation to the region $0 \le r \le 1$ and $0 \le z \le L$, where $L = L_0 / a$. The tube can be either closed at $z = 0$, corresponding to a zero inlet profile in Berman's equation (Fig. 1a), or open, permitting the classic similarity-conforming profile with characteristic speed U_0 (Fig. 1b).[3] Hence, the streamlines can be either induced by the injection process or by the two converging streams. The latter is useful in modeling the flow in hybrid rockets where U_w can be appreciably smaller than U_0 due to slow fuel pyrolysis and fast oxidizer injection. Typical hybrids exhibit values of $U_0 / U_w \sim O(10^2 - 10^3)$ and $M_w = U_w / a_0 \sim O(10^{-4})$, where a_0 is the speed of sound at the origin. Although we concentrate on the interesting case of choked flow at $z = L_s$, the solution will still apply to an isobaric opening when $z < L_s$. In rocketry, the wall Mach number can be as high as 0.02.

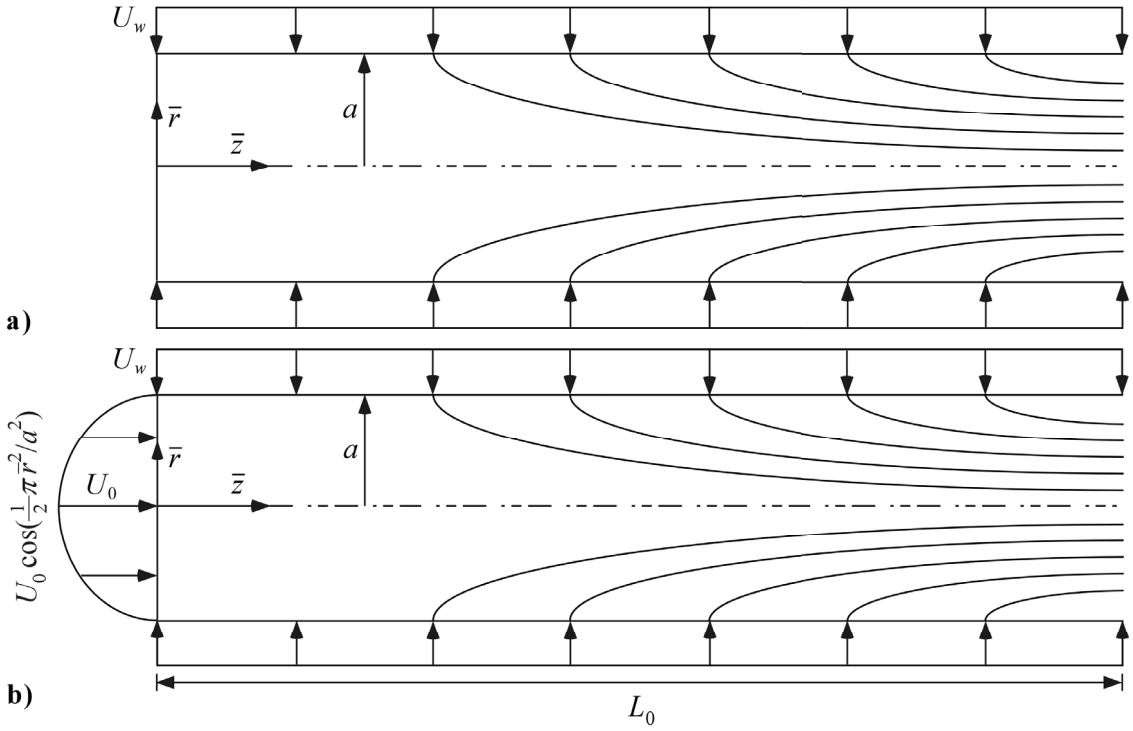

Figure 1. Porous tube accommodating an inlet profile corresponding to a) inert headwall conditions and b) Berman's similarity-conforming cosine distribution.

B. Formulation

We begin by normalizing all remaining variables and operators using standard axisymmetric descriptors. This can be done by setting

$$u_r = \frac{\bar{u}_r}{a_0};\ u_z = \frac{\bar{u}_z}{a_0};\ u_0 = \frac{U_0}{U_w};\ p = \frac{\bar{p}}{p_0};\ T = \frac{\bar{T}}{T_0};\ \rho = \frac{\bar{\rho}}{\rho_0};\ \psi = \frac{\bar{\psi}}{a^2 a_0};\ \boldsymbol{\Omega} = \frac{\bar{\boldsymbol{\Omega}} a}{a_0};\ \nabla = a\bar{\nabla};\ \mathrm{D}^2 = a^2\bar{\mathrm{D}}^2 \tag{1}$$

where the subscript '0' refers to conditions at the origin; $U_0 = \bar{u}_z(0,0)$ and $U_w = -\bar{u}_r(a,\bar{z})$ allude to the injection constants along the headwall and sidewall, respectively. We define the second order linear operator D^2 as

$$\mathrm{D}^2 \equiv \frac{\partial^2}{\partial r^2} - \frac{1}{r}\frac{\partial}{\partial r} + \frac{\partial^2}{\partial z^2} = r\frac{\partial}{\partial r}\left(\frac{1}{r}\frac{\partial}{\partial r}\right) + \frac{\partial^2}{\partial z^2} \tag{2}$$

As usual, the velocity, Stokes streamfunction, and vorticity are related by

$$\boldsymbol{u} = u_r\boldsymbol{e}_r + u_z\boldsymbol{e}_z = -\frac{1}{\rho r}\frac{\partial \psi}{\partial z}\boldsymbol{e}_r + \frac{1}{\rho r}\frac{\partial \psi}{\partial r}\boldsymbol{e}_z;\ \Omega = \Omega_\theta = -\frac{1}{r}\frac{\partial}{\partial z}\left(\frac{1}{\rho}\frac{\partial \psi}{\partial z}\right) - \frac{\partial}{\partial r}\left(\frac{1}{\rho r}\frac{\partial \psi}{\partial r}\right) \tag{3}$$

Moreover, for steady inviscid motion, the momentum equation can be manipulated and reduced to

$$\tfrac{1}{2}\nabla(\boldsymbol{u}\cdot\boldsymbol{u}) - \boldsymbol{u}\times\boldsymbol{\Omega} = -\nabla p/(\rho\gamma) \ \text{ or } \ \tfrac{1}{2}\rho\nabla\left[\nabla\psi\cdot\nabla\psi/(\rho r)^2\right] + (\Omega/r)\nabla\psi = -\nabla p/\gamma \tag{4}$$

where $\gamma \equiv c_p/c_v$. At this stage, the curl of Eq. (4) may be taken to eliminate the pressure and obtain the vorticity transport equation. After grouping and rearranging, one identifies the set of equations that must be solved. These are

$$\nabla\times(\boldsymbol{u}\times\boldsymbol{\Omega}) = -\nabla\rho\times\nabla p/(\gamma\rho^2) \ \text{ (vorticity transport equation)} \tag{5}$$

$$\mathrm{D}^2\psi + \rho r\Omega = \nabla\rho\cdot\nabla\psi/\rho \ \text{ (vorticity equation)} \tag{6}$$

$$\nabla p/\gamma = -\tfrac{1}{2}\rho\nabla\left[\nabla\psi\cdot\nabla\psi/(\rho r)^2\right] - (\Omega/r)\nabla\psi \ \text{ (momentum equation)} \tag{7}$$

Given an isentropic flow of a calorically perfect gas, one also has

$$\rho = p^{1/\gamma} \ \text{ and } \ T = p^{1-1/\gamma} \tag{8}$$

Our auxiliary conditions are prescribed by the continuity of the flow across the centerline and the radial inflow at the sidewall where the streamwise component of the velocity must vanish. Headwall injection can be imposed on the streamwise component in the event of an open boundary. In adherence to the Taylor-Culick model, we begin by considering the case of no flow at $z = 0$. This assortment can be expressed by

$$\begin{cases} \overline{r} = 0,\ \forall \overline{z},\ \overline{u}_r = 0 \text{ (no flow across centerline)} \\ \overline{r} = a,\ 0 \le \overline{z} < L_0,\ \overline{u}_z = 0 \text{ (no slip at sidewall)} \\ \overline{r} = a,\ 0 \le \overline{z} < L_0,\ \overline{u}_r = -U_w \text{ (uniform sidewall injection)} \\ \overline{z} = 0,\ \forall \overline{r},\ \overline{u}_z = 0 \quad \text{(no headwall injection)} \end{cases} \text{ and so } \begin{cases} u_r(0,z) = 0 \\ u_z(1,z) = 0 \\ u_r(1,z) = -M_w \\ u_z(r,0) = 0 \end{cases} \tag{9}$$

Equations (5)–(8) must be solved sequentially according to the following strategy. In order to satisfy the vorticity transport equation, a relation between Ω and ψ must first be determined. This relation is needed in the vorticity equation to eliminate Ω and render a second order PDE in ψ. A solution that satisfies Eq. (9) may then be obtained and returned to the momentum equation so the pressure is deduced. Isentropic relations could then be invoked to calculate the density and temperature. This procedure must be applied after perturbing the system.

C. Perturbation Expansion

Using a Rayleigh-Janzen series in powers of M_w^2 we expand each variable according to

$$\begin{aligned} u_r(r,z) &= M_w u_r^{(0)} + M_w^3 u_r^{(1)} + O(M_w^5) \\ u_z(r,z) &= M_w u_z^{(0)} + M_w^3 u_z^{(1)} + O(M_w^5) \\ \psi(r,z) &= M_w \psi^{(0)} + M_w^3 \psi^{(1)} + O(M_w^5) \\ \Omega(r,z) &= M_w \Omega^{(0)} + M_w^3 \Omega^{(1)} + O(M_w^5) \end{aligned} \quad \text{and} \quad \begin{aligned} \rho(r,z) &= 1 + M_w^2 \rho^{(1)} + M_w^4 \rho^{(2)} + O(M_w^6) \\ p(r,z) &= 1 + M_w^2 p^{(1)} + M_w^4 p^{(2)} + O(M_w^6) \\ T(r,z) &= 1 + M_w^2 T^{(1)} + M_w^4 T^{(2)} + O(M_w^6) \end{aligned} \tag{10}$$

The leading and first order velocity components can be readily obtained at even powers in M_w, specifically

$$M_w: \qquad u_r^{(0)} = -\frac{1}{r}\frac{\partial \psi^{(0)}}{\partial z} \qquad u_z^{(0)} = \frac{1}{r}\frac{\partial \psi^{(0)}}{\partial r} \tag{11}$$

$$M_w^3: \qquad u_r^{(1)} = \frac{\rho^{(1)}}{r}\frac{\partial \psi^{(0)}}{\partial z} - \frac{1}{r}\frac{\partial \psi^{(1)}}{\partial z} \qquad u_z^{(1)} = \frac{1}{r}\frac{\partial \psi^{(1)}}{\partial r} - \frac{\rho^{(1)}}{r}\frac{\partial \psi^{(0)}}{\partial r} \tag{12}$$

On substituting Eq. (10) into Eqs. (5)–(8), we collect, at $o(M_w)$,

$$M_w^2: \qquad \nabla \times [\boldsymbol{u}^{(0)} \times \boldsymbol{\Omega}^{(0)}] = 0 \tag{13}$$

$$M_w: \qquad \mathrm{D}^2 \psi^{(0)} + r\Omega^{(0)} = 0 \tag{14}$$

$$M_w^2: \qquad \nabla p^{(1)} = -\gamma \{\tfrac{1}{2}\nabla[\nabla \psi^{(0)} \cdot \nabla \psi^{(0)} / r^2] + [\Omega^{(0)} / r]\nabla \psi^{(0)}\} \tag{15}$$

$$M_w^2: \qquad \rho^{(1)} = p^{(1)} / \gamma \qquad T^{(1)} = (\gamma - 1) p^{(1)} / \gamma \tag{16}$$

Expansion of Eq. (9) yields, in turn:

$$\begin{cases} u_r^{(0)}(0,z) = 0 \quad \text{(a)}; \quad u_z^{(0)}(1,z) = 0 \quad \text{(b)}; \quad u_r^{(0)}(1,z) = -1 \quad \text{(c)}; \quad u_z^{(0)}(r,0) = 0 \quad \text{(d)} \\ \dfrac{\partial \psi^{(0)}(0,z)}{\partial z} = 0 \left(\text{and } \dfrac{\partial^2 \psi^{(0)}(0,z)}{\partial r \partial z} = 0 \right) \text{(a)}; \ \dfrac{\partial \psi^{(0)}(1,z)}{\partial r} = 0 \text{ (b)}; \ \dfrac{1}{r}\dfrac{\partial \psi^{(0)}(1,z)}{\partial z} = 1 \text{ (c)}; \ \dfrac{\partial \psi^{(0)}(r,0)}{\partial r} = 0 \quad \text{(d)} \end{cases} \tag{17}$$

and so on; at $o(M_w^3)$, we segregate

$$M_w^4: \qquad \nabla \times [\boldsymbol{u}^{(0)} \times \boldsymbol{\Omega}^{(1)}] + \nabla \times [\boldsymbol{u}^{(1)} \times \boldsymbol{\Omega}^{(0)}] = -\nabla \rho^{(1)} \times \nabla p^{(1)} / \gamma \tag{18}$$

$$M_w^3: \qquad \mathrm{D}^2 \psi^{(1)} + r\Omega^{(1)} = \nabla \rho^{(1)} \cdot \nabla \psi^{(0)} - r\rho^{(1)}\Omega^{(0)} \tag{19}$$

$$\begin{aligned} M_w^4: \qquad \nabla p^{(2)} = -\tfrac{1}{2}\gamma (& \rho^{(1)} \nabla [\nabla \psi^{(0)} \cdot \nabla \psi^{(0)} / r^2] - \nabla [\nabla \psi^{(0)} \cdot \nabla \psi^{(1)} / r^2] \\ & + \nabla \{\rho^{(1)} [\nabla \psi^{(0)} \cdot \nabla \psi^{(0)} / r^2]\} - [\Omega^{(0)} \nabla \psi^{(1)} + \Omega^{(1)} \nabla \psi^{(0)}] / r) \end{aligned} \tag{20}$$

$$M_w^4: \qquad \rho^{(2)} = \{2\gamma p^{(2)} + (1-\gamma)[p^{(1)}]^2\} / (2\gamma^2) \text{ and } T^{(2)} = (\gamma - 1)\{2\gamma p^{(2)} - [p^{(1)}]^2\} / (2\gamma^2) \tag{21}$$

For this system, we invoke homogenous boundary conditions to avoid disturbing the leading order approximation which alone must secure the four chief requirements.

III. Solution

A. Basic Analysis

Equations (13)–(17) can be solved consecutively to yield the classic Taylor-Culick solution. To sketch this, we first recall that the vorticity transport relation may be satisfied using $\Omega^{(0)} = C^2 r\psi^{(0)}$. This expression is then fed into Eq. (14) to obtain $\mathrm{D}^2\psi^{(0)} + C^2 r^2\psi^{(0)} = 0$. An incompressible solution that fulfills the problem's constraints ensues for $C = \pi$, namely, $\psi^{(0)} = z\sin(\frac{1}{2}\pi r^2)$. With the replacement of $\psi^{(0)}\nabla\psi^{(0)}$ by $\frac{1}{2}\nabla[\psi^{(0)}]^2$ in the last member of Eq. (15), the basic momentum equation can be integrated into

$$p^{(1)} = -\tfrac{1}{2}\gamma\{\nabla\psi^{(0)}\cdot\nabla\psi^{(0)}/r^2 + [\pi\psi^{(0)}]^2\} = \tfrac{1}{2}\gamma(\pi^2 z^2 + r^{-2}\sin^2\eta)\,;\ \eta \equiv \tfrac{1}{2}\pi r^2 \tag{22}$$

The companion density and temperature are tenable directly from Eq. (16). A simple division by γ yields, for example, $\rho^{(1)} = \frac{1}{2}(\pi^2 z^2 + r^{-2}\sin^2\eta)$.

B. First Order Vorticity Streamfunction Relation

We begin by determining a pivotal relation between $\Omega^{(1)}$ and $\psi^{(1)}$ that satisfies the vorticity transport equation. Since the momentum equation is only used to solve for the pressure, it is vital that Eq. (18) be first secured. In view of the isentropic relation given by Eq. (16), the baroclinic term $\nabla\rho^{(1)}\times\nabla p^{(1)}$ vanishes. We are left with

$$\nabla\times[\boldsymbol{u}^{(0)}\times\boldsymbol{\Omega}^{(1)}] + \nabla\times[\boldsymbol{u}^{(1)}\times\boldsymbol{\Omega}^{(0)}] = 0 \tag{23}$$

The scalar projection of this vector yields a single component, namely,

$$\frac{\partial(u_r{}^{(0)}\Omega^{(1)})}{\partial r} + \frac{\partial(u_z{}^{(0)}\Omega^{(1)})}{\partial z} + \frac{\partial(u_r{}^{(1)}\Omega^{(0)})}{\partial r} + \frac{\partial(u_z{}^{(1)}\Omega^{(0)})}{\partial z} = 0 \tag{24}$$

We now insert Eqs. (11)–(12) into Eq. (24) and use $\Omega^{(0)} = \pi^2 r\psi^{(0)}$. After expanding and simplifying, we collect

$$\frac{\partial\psi^{(0)}}{\partial z}\left(\frac{\Omega^{(1)}}{r} - \frac{\partial\Omega^{(1)}}{\partial r}\right) + \frac{\partial\psi^{(0)}}{\partial r}\frac{\partial\Omega^{(1)}}{\partial z} = -\pi^2 r\left\{\psi^{(0)}\left[\frac{\partial\rho^{(1)}}{\partial r}\frac{\partial\psi^{(0)}}{\partial z} - \frac{\partial\rho^{(1)}}{\partial z}\frac{\partial\psi^{(0)}}{\partial r}\right] + \frac{\partial\psi^{(1)}}{\partial r}\frac{\partial\psi^{(0)}}{\partial z} - \frac{\partial\psi^{(1)}}{\partial z}\frac{\partial\psi^{(0)}}{\partial r}\right\} \tag{25}$$

At first glance, Eq. (25) appears to be staggeringly complex, thereby intractable by known methods. However, taking a cue from the leading order relation for the vorticity, we realize that a solution may mirror the incompressible form within a linear correction. So we let

$$\Omega^{(1)} = \pi^2 r\psi^{(1)} + \Omega_c^{(1)} \tag{26}$$

We find that the first order vorticity transport equation will indeed be satisfied by eliminating the residual

$$\frac{\partial\psi^{(0)}}{\partial z}\left[\frac{\Omega_c^{(1)}}{r} - \frac{\partial\Omega_c^{(1)}}{\partial r}\right] + \frac{\partial\psi^{(0)}}{\partial r}\frac{\partial\Omega_c^{(1)}}{\partial z} = -\pi^2 r\psi^{(0)}\left[\frac{\partial\rho^{(1)}}{\partial r}\frac{\partial\psi^{(0)}}{\partial z} - \frac{\partial\rho^{(1)}}{\partial z}\frac{\partial\psi^{(0)}}{\partial r}\right] \tag{27}$$

or

$$\sin\eta\left[\frac{\Omega_c^{(1)}}{r} - \frac{\partial\Omega_c^{(1)}}{\partial r}\right] + \pi rz\cos\eta\frac{\partial\Omega_c^{(1)}}{\partial z} = -\pi^2 r^{-2} z\sin\eta\left[\sin^3\eta + \pi r^2\cos\eta\left(\pi^2 r^2 z^2 - \sin^2\eta\right)\right] \tag{28}$$

Equation (28) represents a first order PDE in $\Omega_c^{(1)}$ that can be suitably integrated. After some effort, we recoup the general form

$$\Omega_c^{(1)} = -\tfrac{1}{2}\pi^2 r^{-1}(\sin^2\eta + \pi^2 r^2 z^2)\psi^{(0)} + rG[\psi^{(0)}] \tag{29}$$

where $G[\psi^{(0)}]$ is arbitrary.

C. First Order Vorticity Equation

With $\Omega^{(1)}$ at hand, we turn our attention to Eq. (19). With appropriate substitutions, we extract

$$\begin{aligned}\mathrm{D}^2\psi^{(1)} + \pi^2 r^2\psi^{(1)} &= \tfrac{1}{4}\pi r^{-2}\psi^{(0)}\left\{-4\pi r^2 + 2\sin(2\eta) - 4\pi r^2\cos(2\eta) + 4\pi^3 r^4 z^2 - (4/\pi)r^4 G[\psi^{(0)}]/\psi^{(0)}\right\} \\ &= \tfrac{1}{4}\pi^2 z\sin\eta\left\{-4 + \sin(2\eta)/\eta - 4\cos(2\eta) + 8\pi\eta z^2 - (8/\pi^3)\eta G(z\sin\eta)/(z\sin\eta)\right\}\end{aligned} \tag{30}$$

To make further headway, it is expedient to apply the transformation $\psi^{(1)} = F(\eta, z)\sin\eta$. After some algebra, we hold

$$\eta^2\frac{\partial^2 F}{\partial\eta^2} + 2\eta^2\cot\eta\frac{\partial F}{\partial\eta} + \frac{\eta}{2\pi}\frac{\partial^2 F}{\partial z^2} = q(\eta, z) \tag{31}$$

where $$q(\eta,z)=\tfrac{1}{8}\pi\eta z\left\{-4+\sin(2\eta)/\eta-4\cos(2\eta)+8\pi\eta z^2-(8/\pi^3)\eta G(z\sin\eta)/(z\sin\eta)\right\} \tag{32}$$

Without loss in generality, we now let

$$G=\pi^3\left(A_0+A_1 z\sin\eta+A_2 z^2\sin^2\eta+\pi A_3 z^3\sin^3\eta\right) \tag{33}$$

and so

$$q=\tfrac{1}{8}\pi\eta z\left\{-4+\sin(2\eta)/\eta-4\cos(2\eta)-8A_0\eta\csc\eta/z-8A_1\eta-8A_2\eta z\sin\eta+4\pi\eta z^2[2-A_3+A_3\cos(2\eta)]\right\} \tag{34}$$

The problem is ready to be handled. The next step is to introduce a general solution of the form

$$F(\eta,z)=z^3 f(\eta)+z g(\eta) \tag{35}$$

Substitution into Eq. (31) reveals that solvability is possible when $A_0=A_2=0$. We recover two simultaneous ODEs,

$$\eta^2 f''+2\eta^2\cot\eta f'=\tfrac{1}{2}\pi^2\eta^2\left[2-A_3+A_3\cos(2\eta)\right] \tag{36}$$

$$\eta^2 g''+2\eta^2\cot\eta g'=\pi\eta\left\{\tfrac{1}{8}\sin(2\eta)/\eta-\tfrac{1}{2}\left[\cos(2\eta)+1\right]-A_1\eta-3f/\pi^2\right\} \tag{37}$$

where the prime denotes differentiation with respect to η. Being linear, the resulting set is straightforward to manage. We obtain

$$f=\tfrac{1}{8}\cot\eta\left[\pi^2\eta\left(3A_3-4\right)-8C_1\right]+C_2-\tfrac{1}{16}A_3\pi^2\cos(2\eta) \tag{38}$$

$$\begin{aligned} g=\tfrac{1}{64}\pi^{-1}&(3A_3\pi^2\mathrm{Ci}(4\eta)\cot\eta+\mathrm{Ci}(2\eta)\{96C_1-2[(4+3A_3)\pi^2+48C_2]\cot\eta\}\\ &+2\pi\{6(4-3A_3)\pi\eta+32C_4+[\pi(12-9A_3+16A_1\eta)-32C_3]\cot\eta\}\\ &+\{96C_1+[(8+3A_3)\pi^2+96C_2]\cot\eta\}\ln\eta-16(\pi^2+6C_2+6C_1\cot\eta)\mathrm{Si}(2\eta)+3A_3\pi^2\mathrm{Si}(4\eta)) \end{aligned} \tag{39}$$

Here Si and Ci are the fast converging Sine and Cosine Integral functions. They are given by

$$\mathrm{Si}(x)=\int_0^x t^{-1}\sin t\,\mathrm{d}t=x-\tfrac{1}{18}x^3+\tfrac{1}{600}x^5-\tfrac{1}{35280}x^7+O(x^9) \tag{40}$$

$$\mathrm{Ci}(x)=\int_\infty^x t^{-1}\cos t\,\mathrm{d}t=\mathfrak{E}+\ln x-\tfrac{1}{4}x^2+\tfrac{1}{96}x^4-\tfrac{1}{4320}x^6+O(x^8);\quad \mathfrak{E}\simeq 0.577216 \text{ (Euler's Gamma constant)} \tag{41}$$

D. Undetermined Constants and Vital Boundary Conditions

Our general solution $\psi^{(1)}=z(z^2 f+g)\sin\eta$ contains a set of 6 unknown constants, $(A_1,A_3,C_1,C_2,C_3,C_4)$. This is not an overly determined system but rather consistent with Eq. (9). Out of the four existing boundary conditions,

$$u_r^{(1)}(0,z)=0\quad\text{(a)};\quad u_z^{(1)}(1,z)=0\qquad\text{(b)};\quad u_r^{(1)}(1,z)=0\quad\text{(c)};\quad u_z^{(1)}(r,0)=0\quad\text{(d)} \tag{42}$$

only three are useful. The fourth, $u_z^{(1)}(r,0)=0$ is identically satisfied by $\psi^{(1)}$ at $z=0$. The three remaining statements (a–c) yield six constraints in integer powers of z (that must vanish independently). The two additional constants (one could have expected four) are therefore essential. As noted by Balakrishnan, Liñan and Williams[29] this problem is quasi-parabolic. To illustrate this behavior, we first consider Eq. (42)a that conveys into

$$r=0,\forall z:\qquad \frac{\partial\psi^{(1)}}{\partial z}-\rho^{(1)}\frac{\partial\psi^{(0)}}{\partial z}=0\qquad\text{and}\qquad \frac{\partial}{\partial r}\left[\frac{\partial\psi^{(1)}}{\partial z}-\rho^{(1)}\frac{\partial\psi^{(0)}}{\partial z}\right]=0 \tag{43}$$

Its evaluation begets two equations at $O(1)$ and $O(z^2)$ that must cancel simultaneously. The first one reads

$$64\pi C_3+96C_2(\ln 2+\mathfrak{E})+\pi^2[8\ln 2-24+8\mathfrak{E}+3A_3(6+\mathfrak{E})]=0 \tag{44}$$

while the second leads to $C_1=0$.

To ensure no slippage and uniform inflow along the sidewall, we must enforce $u_z^{(1)}(1,z)=u_r^{(1)}(1,z)=0$. In terms of the streamfunction, we now write

$$r=1,\forall z:\qquad \frac{\partial\psi^{(1)}}{\partial r}-\rho^{(1)}\frac{\partial\psi^{(0)}}{\partial r}=0\qquad\text{and}\qquad \frac{\partial\psi^{(1)}}{\partial z}-\rho^{(1)}\frac{\partial\psi^{(0)}}{\partial z}=0 \tag{45}$$

This set engenders four equations in descending orders of z. By canceling the $O(z^3)$, $O(z^2)$ and $O(1)$ terms, we successively gather $A_3=\frac{4}{3}$, $C_2=-\frac{1}{4}\pi^2$ and $C_4=-\frac{1}{2}-\frac{1}{16}\pi[\mathrm{Si}(2\pi)+2\mathrm{Si}(\pi)]\simeq -1.50571$. Finally, at $O(z)$ we reap

$$4A_1\pi-16C_3/\pi-3\ln(\tfrac{1}{2}\pi)+\mathrm{Ci}(2\pi)+2\mathrm{Ci}(\pi)=0 \tag{46}$$

Equation (44) may be revisited to pick $C_3=\frac{1}{16}\pi(4\ln 2+3\mathfrak{E})\simeq 0.884405$. This enables us to calculate the last constant from Eq. (46), namely, $A_1=[\ln 2\pi^3+3\mathfrak{E}-\mathrm{Ci}(2\pi)-2\mathrm{Ci}(\pi)]/(4\pi)\simeq 0.456314$. We thus conclude our derivation of a fully axisymmetric solution that exactly satisfies Eqs. (18)–(19).

IV. Results and Discussion

The compressible correction may be rearranged and simplified with the net product taking the form of a rather straightforward expression. It collapses into

$$\psi^{(1)} = \tfrac{1}{4}\pi z \sin\eta\left(-\pi z^2\left[1+\tfrac{1}{3}\cos(2\eta)\right] + \tfrac{1}{4}\left\{\mathrm{Si}(4\eta)+2\mathrm{Si}(2\eta)-\alpha+\left[\beta r^2 - 3\mathscr{E} + \mathrm{Ci}(4\eta)+2\mathrm{Ci}(2\eta)-\ln(2\pi^3 r^6)\right]\cot\eta\right\}\right) \tag{47}$$

where $\alpha = 8/\pi + \mathrm{Si}(2\pi) + 2\mathrm{Si}(\pi) \simeq 7.6685048$ and $\beta = \ln(2\pi^3) + 3\mathscr{E} - \mathrm{Ci}(2\pi) - 2\mathrm{Ci}(\pi) \simeq 5.7342087$. Equation (47) will be referred to as the 'exact' solution. Upon closer scrutiny, we identify an approximate form $\tilde{\psi}^{(1)}$ that is practically equivalent in spatial behavior due to the dominance of the third power in z; we thus unveil

$$\tilde{\psi}^{(1)} = -\tfrac{1}{4}\psi^{(0)}\left\{\pi^2 z^2\left[1+\tfrac{1}{3}\cos(2\eta)\right]+2\right\} \text{ or } \tilde{\psi} = M_w\psi^{(0)}\left(1-\tfrac{1}{4}M_w^2\left\{\pi^2 z^2\left[1+\tfrac{1}{3}\cos(\pi r^2)\right]+2\right\}\right) \tag{48}$$

Equation (48) represents the simplest axisymmetric form that satisfies the problem's four boundary conditions while exhibiting a high degree of precision in observing first principles. It accrues a negligible error in comparison with $\psi^{(1)}$ to the extent of being graphically indiscernible from Eq. (47). Furthermore, the error continues to diminish with the distance from the headwall. It is hence idyllically suited to model long porous tubes such as those used to simulate rocket chambers. In making our choice, the exact solution will be utilized in graphical depictions although, for added confirmation, $\tilde{\psi}^{(1)}$ will be carried alongside $\psi^{(1)}$ during the upcoming development. In actuality, $\tilde{\psi}^{(1)}$ may serve as a crucial replacement in applications where simplicity of the mean flow formula is essential in preventing a purely numerical outcome (e.g., those involving integration).

A. Representative Streamlines

Figure 2 compares the flow turning behavior with and without compressibility at two wall Mach numbers and chamber lengths. Here we plot the characteristic ψ/M_w. The first observation is that compressibility causes the fluid to turn more sharply at a given location and that the streamline curvature is steepened with successive increases in M_w. This effect has important implications on flow stability.[38] In fact, it appears that fluid expansion in the downstream direction has a similar effect to that of increasing the viscosity. As illustrated before,[20] decreasing the wall Reynolds number has a similar injunction on the flow. Incorporating both density changes and viscosity may therefore lead to more pronounced steepening. Viscosity, which has often been neglected in SRM simulations, may become an important factor in hybrid rocket analysis where the wall Reynolds number is considerably smaller. We mention in passing that, for simulated SRMs, wall expansion has been shown to exhibit the reverse effect on curvature, albeit too small to be considered except for extremely large regression rates. A purely hypothetical case occurs when the sidewall regresses at the same speed as that of the fluid entering the tube. Under these auspices, the expansion process can offset the effect of injection to such a degree that streamlines become normal to the sidewall.

The second observation in Fig. 2 concerns the striking similarity between parts a and b and the connection with the corresponding ratio of Mach numbers and chamber lengths. As M_w is reduced by half in Fig. 2b, note that it takes the streamlines twice the distance to reach the same level of development and disparity with respect to the Taylor solution. This trend insinuates that a direct relation may exist between M_w and the length to reach a level of development. The plot also suggests that compressibility effects may not be large in short chambers unless M_w is sufficiently high, particularly, exceeding a threshold value that may be helpful to determine. Finding the choking distance is another critical requirement for the purpose of delimiting the subsonic domain.

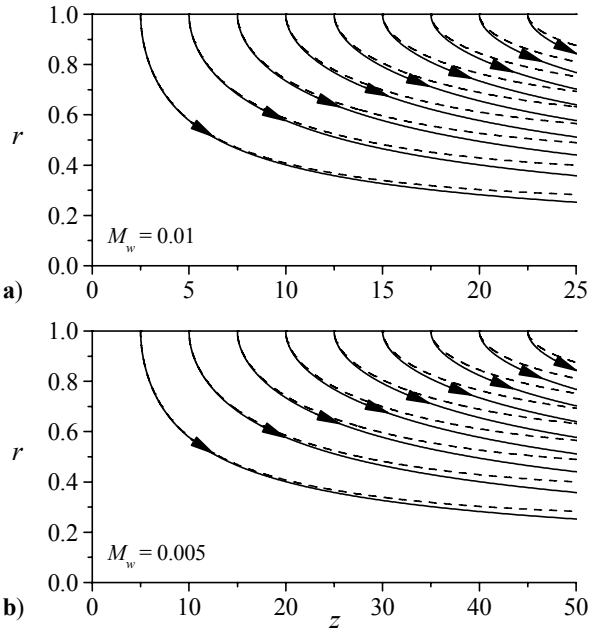

Figure 2. Effect of compressibility on representative streamlines. Unless stated otherwise, we use γ = 1.4 and lines —— or dashes - - - - to denote incompressible and compressible solutions, respectively.

B. Velocity and Vorticity Fields

Velocity corrections can be derived starting from Eq. (12). We obtain

$$u_r^{(1)} = \tfrac{1}{16} r^{-3}(\sin\eta\{2\eta(2\pi z^2+\alpha)-6-2\eta[\mathrm{Si}(4\eta)+2\mathrm{Si}(2\eta)]\}+2(2\pi\eta z^2+1)\sin(3\eta)$$
$$+2\eta\cos\eta[3\mathfrak{C}-\beta r^2-\mathrm{Ci}(4\eta)-2\mathrm{Ci}(2\eta)+\ln(2\pi^3 r^6)]) \quad (49)$$

$$u_z^{(1)} = \tfrac{1}{48}\pi z(\cos\eta\{14\pi^2 z^2-3\pi\alpha+6\beta+3\pi[\mathrm{Si}(4\eta)+2\mathrm{Si}(2\eta)]\}-6\pi^2 z^2\cos(3\eta)$$
$$+3\pi\sin\eta[3\mathfrak{C}-\beta r^2-\mathrm{Ci}(4\eta)-2\mathrm{Ci}(2\eta)+\ln(2\pi^3 r^6)]) \quad (50)$$

Then, using $\Omega^{(0)} = \pi^2 rz\sin\eta$, the first order vorticity may be expressed by

$$\Omega^{(1)} = \tfrac{1}{16} r^{-2}\Omega^{(0)}\{2(1-6\pi\eta z^2)(3-4\sin^2\eta)-6+r^2(\tfrac{14}{3}\pi^2 z^2-\pi\alpha+4\beta)+2\eta[\mathrm{Si}(4\eta)+2\mathrm{Si}(2\eta)]$$
$$+2\eta\cot\eta[\beta r^2-3\mathfrak{C}+\mathrm{Ci}(4\eta)+2\mathrm{Ci}(2\eta)-\ln(2\pi^3 r^6)]\} \quad (51)$$

Recalling the classic solution, $\boldsymbol{u}^{(0)} = -r^{-1}\sin\eta\boldsymbol{e}_r + \pi z\cos\eta\boldsymbol{e}_z$, the approximate velocity can be assembled into

$$\tilde{\boldsymbol{u}}^{(1)} = -\tfrac{1}{4}u_r^{(0)}\{\pi^2 z^2[\cos(2\eta)+1]+r^{-2}[\cos(2\eta)-1]+2\}\boldsymbol{e}_r + \tfrac{1}{12}u_z^{(0)}\{\pi^2 z^2[5-3\cos(2\eta)]+3r^{-2}[1-\cos(2\eta)]-6\}\boldsymbol{e}_z \quad (52)$$

and so $\tilde{\Omega}^{(1)} = \pi r^{-3} z\sin\eta\cos\eta(\sin\eta+2\eta\cos\eta)$. The total vorticity becomes

$$\tilde{\Omega} = M_w\Omega^{(0)}[1+M_w^2 r^{-2}\cos\eta(\cos\eta+\tfrac{1}{2}\sin\eta/\eta)] \quad (53)$$

As usual, the vorticity vanishes along the centerline and, by observing surface adherence, is maximum at the sidewall. It can be calculated from

$$\Omega_w = M_w\pi^2 z[1+M_w^2(\tfrac{2}{3}\pi^2 z^2+\tfrac{1}{4}\beta-1)] \quad \text{or} \quad \tilde{\Omega}_w = M_w\pi^2 z(1+\tfrac{2}{3}M_w^2\pi^2 z^2) \quad (54)$$

The last two expressions differ by a mere $\pi^2 z M_w^3(\frac{1}{4}\beta-1)$. This reflects the inherent accuracy that accompanies our compact formula. As it builds up with successive increases in z, Ω_w reaches its highest value in the exit plane.

Typical profiles corresponding to Fig. 2a are illustrated in Fig. 3; here, we plot both streamwise and radial components of velocity at six axial stations, $\gamma = 1.4$, and a characteristic Mach number of 0.01. We choose the latter because of its proximity to $M_w = 0.0095$, a figure that has been fixed in two separate studies; these include Apte and Yang[18,19] who added much insight to the elegant work of Traineau, Hervat and Kuentzmann.[13] Incidentally, both groups have focused on cold-flow compressible simulations and laboratory experiments of the planar, porous channel case with air injection. We hereby select the same values in the interest of uniformity and portability. Lower injection rates from 0.0018 to 0.0036 have also been investigated by Dunlap and coworkers.[39]

In Fig. 3, it is clear that the discrepancy with respect to the leading order solution increases with the distance from the headwall. In both plots, this difference is hardly noticeable before crossing nearly one-third of the chamber span. Subsequently, the error in the Taylor-Culick model becomes progressively more pronounced, especially after passing $z = 15$. Both streamwise and radial profiles begin to flatten, precisely as predicted by numerical simulations and experimental evidence. By $z = 25$, the error between both models, taken at the centerline, reaches about 10%.

In order to better understand the factors that influence our solution, we find it imperative to calculate the point where the Mach number reaches unity. To this end, we define the length L_s to be the distance along the centerline to the point where a sonic condition is met. We base our definition on the idea of a local Mach number instead of an area-averaged value. The latter is necessitated by one-dimensional or pseudo-two-dimensional models where information is often lumped at a given cross-section. Bearing this in mind, we remark that when $z = L_s$, only the centerline velocity component would have reached the speed of sound. At this junction, the area-averaged Mach number will be smaller than unity. In order to precisely determine the sonic point, we realize that the temperature

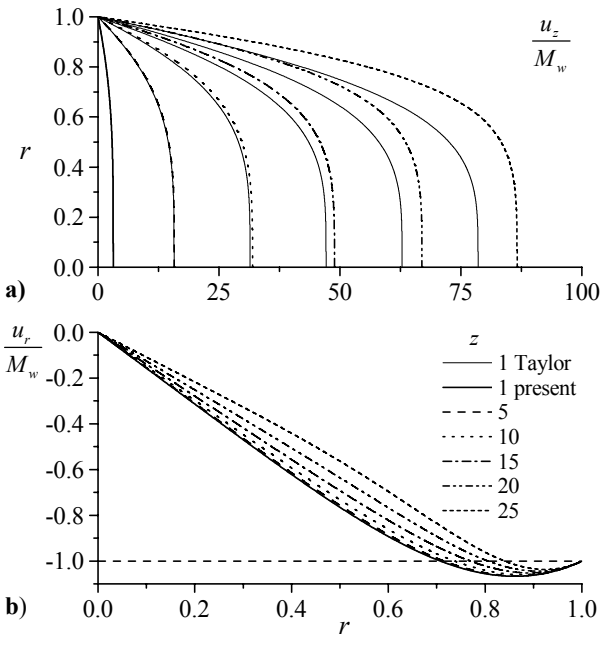

Figure 3. Spatial evolution of axial and radial velocities for M_w = 0.01. The compressible solution leads with respect to the Taylor-Culick marker lines.

correction must be evaluated to accurately estimate the local a_0. In this vein, the momentum equation must first be solved for the higher order pressure correction. We do this for the sake of completeness, although higher order pressures and temperatures are not likely to be large contributors except in long chambers.

C. Higher Order Pressures and Temperatures

In seeking the higher order pressure term, we return to Eq. (20) whose right-hand-side is now fully determined. We write

$$\nabla p^{(2)} = -\tfrac{1}{2}\gamma(\rho^{(1)}\nabla[\nabla\psi^{(0)}\cdot\nabla\psi^{(0)}/r^2]-\nabla[\nabla\psi^{(0)}\cdot\nabla\psi^{(1)}/r^2] \\ +\nabla\{\rho^{(1)}[\nabla\psi^{(0)}\cdot\nabla\psi^{(0)}/r^2]\}-[\Omega^{(0)}\nabla\psi^{(1)}+\Omega^{(1)}\nabla\psi^{(0)}]/r) \tag{55}$$

Partial integration must be carefully carried out to identify common terms in both radial and streamwise directions. It is expedient to start with the approximate solution as the process can help in verifying the final formulation. After some algebra, we obtain $\tilde{p}^{(2)}/\gamma = -\frac{1}{24}\pi^4 z^4 + \frac{1}{8}\pi^2 z^2(4-\pi\eta) + \frac{1}{32}\pi\eta(8-3\pi\eta)$. Backward substitution into the perturbed pressure yields

$$\tilde{p}/\gamma = \gamma^{-1} - \tfrac{1}{2}\pi^2 M_w^2 z^2[1+(\tfrac{1}{4}\pi\eta-1)M_w^2] - \tfrac{1}{24}\pi^4 M_w^4 z^4 - \tfrac{1}{4}\pi M_w^2 \sin^2\eta/\eta + \tfrac{1}{32}\pi^2 M_w^4\eta(8/\pi-3\eta) \tag{56}$$

Along similar lines, we find

$$p^{(2)}/\gamma = -\tfrac{1}{24}\pi^4 z^4 + \tfrac{1}{16}\pi^2 z^2(\sigma-2\pi\eta) + \tfrac{1}{32}\pi^2\eta(\sigma/\pi-5\eta) \tag{57}$$

where $\sigma = \pi\alpha - 2\beta \simeq 12.6229$. It is clear that the pressure is dominated by $p \sim 1-\frac{1}{2}\pi^2\gamma M_w^2 z^2 - \frac{1}{24}\pi^4 M_w^4 z^4$. This series can be further confirmed by calculating the centerline pressure ratio p_c. In fact, we find $\tilde{p}_c = 1-\frac{1}{2}\pi^2\gamma M_w^2 z^2(1-M_w^2) - \frac{1}{24}\pi^4\gamma M_w^4 z^4$ to be in perfect unison with

$$p_c = 1-\tfrac{1}{2}\pi^2\gamma M_w^2 z^2(1-\tfrac{1}{8}\sigma M_w^2) - \tfrac{1}{24}\pi^4\gamma M_w^4 z^4 \tag{58}$$

The higher order density and temperature can be evaluated from Eq. (21). The latter may be arranged into

$$T = 1+\tfrac{1}{8}\pi(\gamma-1)M_w^2\{-4\pi z^2+\eta^{-1}[\cos(2\eta)-1]\} + M_w^4 T^{(2)} \tag{59}$$

where $T^{(2)}$ is given by

$$\tilde{T}^{(2)} = -\tfrac{1}{6}\pi^2(\gamma-1)\{\pi^2 z^4 + \tfrac{3}{8}\pi\eta^{-1}z^2[1-\cos(2\eta)-8\eta/\pi+2\eta^2] + \tfrac{3}{128}\eta^{-2}[3-4\cos(2\eta)+\cos(4\eta)-64\eta^3/\pi+24\eta^4]\} \tag{60}$$

or

$$T^{(2)} = -\tfrac{1}{6}\pi^2(\gamma-1)\{\pi^2 z^4 + \tfrac{3}{8}\pi\eta^{-1}z^2[1-\cos(2\eta)-\sigma\eta/\pi+2\eta^2] + \eta^{-2}[\tfrac{9}{128}-\tfrac{3}{32}\cos(2\eta)+\tfrac{3}{128}\cos(4\eta)-\tfrac{3}{16}\sigma\eta^3/\pi+\tfrac{15}{16}\eta^4]\} \tag{61}$$

Here too, the temperature is dominated by $T \sim 1-\frac{1}{2}\pi^2(\gamma-1)M_w^2 z^2 - \frac{1}{6}\pi^4(\gamma-1)M_w^4 z^4$. Centerline temperatures yield, in turn, $\tilde{T}_c = 1-\frac{1}{2}\pi^2(\gamma-1)M_w^2 z^2(1-M_w^2) - \frac{1}{6}\pi^4(\gamma-1)M_w^4 z^4$ and

$$T_c = 1-\tfrac{1}{2}\pi^2(\gamma-1)M_w^2 z^2(1-\tfrac{1}{8}\sigma M_w^2) - \tfrac{1}{6}\pi^4(\gamma-1)M_w^4 z^4 \tag{62}$$

These variables are crucial for estimating the maximum Mach number at a given cross section. It may be interesting to remark that approximate results at $\eta = 0$ may be deduced from the exact expressions by replacing σ with 8.

D. Critical Chamber Length

With the temperature in hand, we can calculate the centerline Mach number based on the local speed, viz.

$$u_c = u_z(0,z) = \pi M_w z + \tfrac{1}{6}\pi^3 M_w^3 z^3 - \tfrac{1}{16}\sigma\pi M_w^3 z \text{ or } \tilde{u}_c = \pi M_w z + \tfrac{1}{6}\pi^3 M_w^3 z^3 - \tfrac{1}{2}\pi M_w^3 z \tag{63}$$

Clearly, $u_c \sim \pi M_w z + \frac{1}{6}\pi^3 M_w^3 z^3$ controls the solution. Using $\bar{u}_c/\sqrt{c_p(\gamma-1)\bar{T}_c} = 1$ or $u_c/\sqrt{T_c} = 1$, we can solve for the streamwise coordinate z_s at which a sonic condition is first detected. Depending on the level of approximation in the speed and temperature, we obtain estimates of increasing accuracy. At leading order, we have

$$\pi M_w z_s = \sqrt{1-\tfrac{1}{2}\pi^2(\gamma-1)M_w^2 z_s^2} + O(M_w^3 z_s^3) \text{ or } z_s^{(0)} = \frac{1}{\pi M_w}\sqrt{2/(1+\gamma)} + O(M_w^2 z_s^3) \tag{64}$$

In like manner, by retaining two terms in the velocity, we can put

$$\pi M_w z_s + \tfrac{1}{6}\pi^3 M_w^3 z_s^3 = \sqrt{1-\tfrac{1}{2}\pi^2(\gamma-1)M_w^2 z_s^2} + O(M_w^4 z_s^4) \text{ or } z_s^{(1)} = \frac{1}{\pi M_w}\sqrt{2^{1/3}\varphi - 4 + 2^{2/3}(5-3\gamma)/\varphi} + O(M_w^3 z_s^4) \tag{65}$$

where

$$\varphi = \left[18\gamma - 5 + 3\sqrt{6\gamma(5+\gamma+\gamma^2)-25}\right]^{1/3} \tag{66}$$

To briskly wander off this course, though momentarily, a simple expression can be obtained by 'borrowing' the well-known critical pressure ratio from one-dimensional nozzle theory. By choosing only two terms in Eq. (58), we can equate, at the sonic point –which stands for the hypothetical nozzle throat,

$$(p_c)_{\text{sonic}} = 1 - \tfrac{1}{2}\pi^2\gamma M_w^2 z_s^2 = [\tfrac{1}{2}(\gamma+1)]^{\gamma/(1-\gamma)} \text{ or } z_s^{(2)} = \frac{1}{\pi M_w}\sqrt{2\gamma^{-1}\left[1-\left(\tfrac{1}{2}\gamma+\tfrac{1}{2}\right)^{\gamma/(1-\gamma)}\right]} = \frac{\sqrt{2(1-e^{-1/2})}}{\pi M_w};\gamma = 1 \quad (67)$$

Note that the spurious singularity as $\gamma \to 1$ can be easily overcome using l'Hôpital's rule. However, it is not simple to render the truncation order of this quantity because of the uncertainty associated with utilizing one-dimensional theory to evaluate the critical pressure ratio. No throat of a nozzle exists here. While Eq. (58) exhibits a truncation error of $O(M_w^4 z_s^4)$, the global error accrued in crisscrossing with one-dimensional nozzle theory remains an open question. At this point, a comparison with the most precise value of z_s may be illuminating.

The most accurate representation of $O(M_w^4 z_s^3)$, say $z_s^{(5)}$, may be derived by mustering every term that arises in Eqs. (62) and (63). The lengthy formula we obtain is omitted here as it may be relegated to symbolic programming. Instead, we realize that, within four-digit accuracy, an equivalent expression is attainable by employing the dominant members of the temperature and velocity. We find

$$z_s^{(3)} = \frac{\delta^{1/2}}{\pi M_w}\sqrt{\cos\{\tfrac{1}{3}\cos^{-1}[16(14+6\gamma-3\gamma^2-4\gamma^3)/\delta^3]\}-2(\gamma+1)} + O(M_w^2 z_s); \quad \delta = 2\sqrt{2(\gamma+1)(2\gamma-1)} \quad (68)$$

Or, equivalently,

$$z_s^{(3)} = \frac{1}{\pi M_w}\sqrt{2^{1/3}\lambda - 2\gamma - 2 + 2^{2/3}(2\gamma^2+\gamma-1)/\lambda}\ ;\ \lambda = \left(14+6\gamma-3\gamma^2-4\gamma^3+3\sqrt{22+18\gamma-6\gamma^2-14\gamma^3-3\gamma^4}\right)^{1/3} \quad (69)$$

These supplement the expanded form of $z_s^{(5)}$, namely,

$$z_s^{(4)} = \frac{1}{\pi M_w}[0.8846222 - 0.17729882(\gamma-1) + 0.05391187(\gamma-1)^2 - 0.01806146(\gamma-1)^3 + 0.50162947M_w^2] \quad (70)$$

As it turns out, Eqs. (67), (68) and (70) are the closest to $z_s^{(5)}$. This trend is illustrated in Table 1 where the critical lengths are catalogued at typical Mach numbers and a range of specific heats. We note that the errors we entail are commensurate with the order in which they are introduced. Interestingly, the pseudo-one-dimensional approximation $z_s^{(2)}$ leads to a surprisingly valid estimate that keeps improving at higher M_w. This may explain the ubiquitous acceptance of one-dimensional analyses which, in some work, have been reported to exceed expectations in predicting compressible flow behavior. This is especially true concerning pressure distributions. Depending on the desired tolerances, we recommend the use of $L_s = z_s^{(4)}$ or $z_s^{(3)}$ for small and large γ, respectively. We also post in Table 1 the most precise estimate $z_s^{(5)}$ for 6 representative values of M_w. In that respect, we note that, for $M_w < 0.005$, L_s becomes so large as to render it impractical in propulsive applications that exclude headwall injection; this may explain why choking through a nozzle is the rule rather than the exception in rocket-based applications.

Table 1. Critical sonic length, L_s

γ \ z	$z_s^{(0)}$	$z_s^{(1)}$	$z_s^{(2)}$	$z_s^{(3)}$	$z_s^{(4)}$	$z_s^{(5)}$
	$M_w = 10^{-2}$					
1.0	31.831	28.158	28.237	28.158	28.160	28.160
1.1	31.064	27.719	27.661	27.611	27.612	27.612
1.2	30.350	27.294	27.119	27.094	27.095	27.096
1.3	29.683	26.884	26.610	26.606	26.606	26.607
1.4	29.058	26.488	26.130	26.143	26.140	26.145
5/3	27.566	25.496	24.972	25.020	24.990	25.022
	$M_w = 5\times10^{-3}$					
1.0	63.662	56.317	56.474	56.317	56.318	56.318
1.1	62.128	55.437	55.321	55.221	55.222	55.222
1.2	60.699	54.588	54.239	54.188	54.188	54.189
1.3	59.365	53.768	53.221	53.211	53.209	53.212
1.4	58.115	52.976	52.260	52.286	52.278	52.287
5/3	55.133	50.993	49.943	50.040	49.978	50.041
	$z_s^{(5)}$					
M_w =	0.0001	0.0005	0.001	0.005	0.01	0.05
1.0	2815.840	563.168	281.584	56.318	28.160	5.640
1.1	2761.064	552.213	276.107	55.222	27.612	5.530
1.2	2709.402	541.880	270.940	54.189	27.096	5.427
1.3	2660.569	532.114	266.057	53.212	26.607	5.329
1.4	2614.318	522.864	261.432	52.287	26.145	5.236
5/3	2502.020	500.402	250.201	50.041	25.022	5.011

Past the sonic point, it is uncertain whether our solution will continue to hold. Unless area expansion is permitted, weak shocks are likely to form and these are normally accompanied by irreversibilities; of course, the latter tend to invalidate our underlying assumptions. Barring these incidences, it may be argued that the solution may continue to hold up to the point where the area-averaged Mach number has reached unity. Although we do not wish to venture farther downstream, it may be useful to examine the evolution of the area-averaged

Mach number for two main reasons. Firstly, to set an upper bound on the range of validity and, secondly, to provide supplementary tools that may be needed in sketching a meaningful parallelism with one-dimensional theory.

E. Area Averaging

The local Mach number may be calculated from the total velocity and temperature using $M \equiv u/\sqrt{T}$, where u is the Pythagorean sum of u_r and u_z. Several lines of constant Mach number can thus be produced and displayed in Fig. 4a for $\gamma = 1.4$ and $M_w = 0.01$. Also shown on the plot are a few representative streamlines. What is most intriguing is perhaps our attempt to recreate the same plots using widely dissimilar Mach values of 10^{-3} and 10^{-4}. So long as the streamwise coordinate is rescaled by the appropriate sonic length, L_s, differences remain indiscernible. The same attempt is repeated using, this time, $\gamma = 1$ and $5/3$; differences are found to be so minor that they do not warrant further attention. Figure 4a is hence characteristic of the expected iso-contours. In fact, they bear a striking resemblance to those reported in Fig. 3 of Balakrishnan, Liñan and Williams.[29] We show our streamlines and Mach numbers past the choking distance to illustrate their spatial evolution in the event that a shock is delayed. As mentioned earlier, only the centerline velocity would have reached sonic speed at $z = L_s$ and there is little certainty beyond that point. We recall that, instead of deteriorating past $M = 0.3$, the Taylor model continued to hold farther downstream. The compressible flow analogue may exhibit comparable resilience. Furthermore, the area-averaged Mach number at $z = L_s$ may be calculated and shown to vary quite gradually, specifically, between 0.696 and 0.710 as γ is reduced from $5/3$ to 1. This will be expounded next.

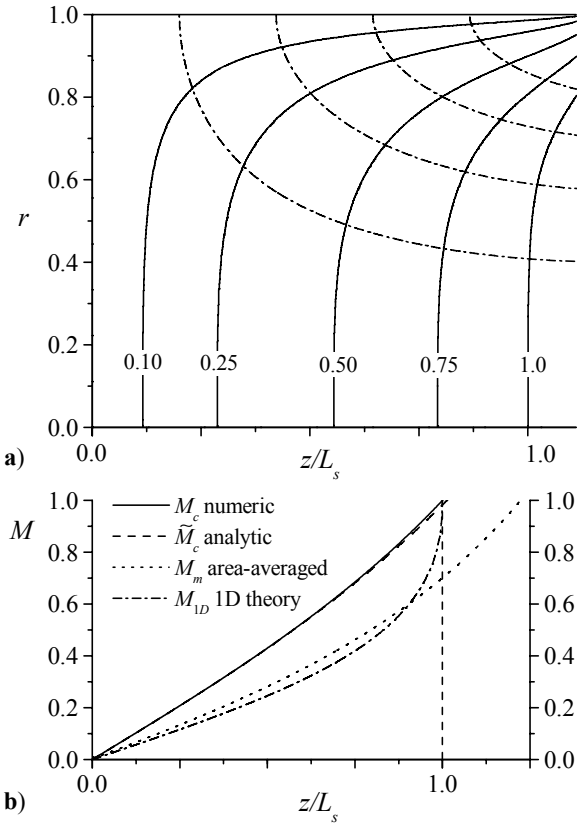

Figure 4. Evolution of the local Mach number over a range of M_w and $\gamma = 1.4$. Contour plots shown in a) extend slightly past the choking distance. Centerline Mach numbers and area-averaged values are compared in b) to the one-dimensional compressible flow formula by Gany and Aharon (1999).[37]

The centerline Mach number $M_c \equiv u_c/\sqrt{T_c}$ can be readily obtained from Eqs. (62)–(63) and plotted in Fig. 4b. Also shown is a crude but compact approximation based on $\tilde{\psi}$ and the first order temperature. We imply

$$\tilde{M}_c = \pi M_w z \frac{2 + M_w^2(\frac{1}{3}\pi^2 z^2 - 1)}{\sqrt{4 - 2M_w^2 \pi^2 z^2 (\gamma - 1)}} \tag{71}$$

One may infer from Fig. 4b that $\tilde{M}_c$ is an adequate representation except for the slight overshoot that it displays near the aft end. As γ is decreased, this discrepancy becomes less conspicuous and vanishes, eventually, near unity.

To set the stage for comparisons with one-dimensional theory, the area-averaged Mach number, M_m, can be numerically integrated from $M_m = 2\int_0^1 uT^{-1/2} r\,\mathrm{d}r$. As shown on the graph, M_m is close to 0.7 and does not reach unity until $z = L_m$. Following a parametric analysis, we find that L_m is a weak function of γ, and practically independent of M_w. It diminishes from $L_m = 1.257L_s$ to $1.204L_s$ as γ is escorted across its full range. Along this excursion, M_c crawls from 1.341 to 1.390. We suspect that full choking in a straight porous tube may be delayed an extra 20-25% of the sonic length. If the opposite were proven true, then the evaluation of M_m would still serve a useful purpose as it enables us to judiciously compare with one-dimensional theory. According to the latter,

$$M_{1D} = \sqrt{\frac{1 - \sqrt{1 - z^2/L_s^2}}{1 + \gamma\sqrt{1 - z^2/L_s^2}}} \tag{72}$$

Equation (72) is superimposed as the chained line in Fig. 4b; clearly it follows M_m except for the sudden sprint in the last 10% stretch. This result is gratifying as it confirms the ability of our solution to mimic one-dimensional

analysis except near the sonic point where radial flow variability comes into play. Our results also support the idea of a local Mach number being independent of M_w.

F. Key Geometric Similarity

Inspired by the form of Eq. (72), a more convincing proof of this behavior may be pursued by introducing a rescaled variable, $X = z/L_s$. One may, for example, substitute back into Eq. (71) and rearrange. As confirmed by Eqs. (64)–(69), the ensuing product $\pi M_w L_s = \Gamma(\gamma) \sim 1$ is a strong function of γ, particularly, one for which several approximations have been unraveled in increasing order of accuracy. It can be seen that

$$\tilde{M}_c = \Gamma(\gamma) X \frac{2 + \frac{1}{3}\Gamma^2(\gamma)X^2 - M_w^2}{\sqrt{4 - 2\Gamma^2(\gamma)X^2(\gamma - 1)}} = \frac{1 + \frac{1}{6}\Gamma^2(\gamma)X^2 - \frac{1}{2}M_w^2}{\sqrt{\Gamma^{-2}(\gamma)X^{-2} - \frac{1}{2}(\gamma - 1)}} \tag{73}$$

The influence of M_w is clearly negligible. Furthermore, the dependence on γ is also feeble in view of the slowly varying filter Γ. The latter shifts by a total of 11%, from 0.8846 to 0.7860, over the full range of γ. In rocketry, γ seldom exceeds 1.2; the corresponding 3.78% deviation in Γ is marginal, being from 88.5 to 85.1% only. As γ barely changes in a given application, the behavior of our solution with respect to X is nearly 'frozen.' This finding is pivotal as it enables us to render the results in a more universal fashion, namely, independently of the wall Mach number. The same idea applies to the streamfunction and its derivatives; this can be demonstrated by revisiting

$$\tilde{\Psi} = \tilde{\psi}/M_w = \psi^{(0)}\left(1 - \tfrac{1}{4}\Gamma^2(\gamma)\left\{X^2\left[1 + \tfrac{1}{3}\cos(\pi r^2)\right] + 2\pi^{-2}L_s^{-2}\right\}\right) \tag{74}$$

Note that dependence on M_w disappears in a suitably normalized variable. Being a parent function, all related family members inherit this property. This also explains and settles our earlier bewilderment regarding the nature of Fig. 3 where, in hindsight, the geometric scaling required to achieve similarity was met (unintentionally). The critical lengths for the two cases were actually 26 and 52, respectively.

G. Critical Pressure and Temperature Ratios

Unlike the local Mach number that can undergo wide excursions at a given cross section, we find the pressures and temperatures to be quasi uniform. This can be quickly inferred from the favorable comparisons that may be drawn between any two of the centerline, sidewall, or area-averaged properties. Due to their similarities, we focus hereafter on centerline behavior (see Fig. 5). Our axisymmetric results can also be examined in the context of existing theories. Of those we choose the oft-cited one-dimensional model of Gany and Aharon,[37] the pseudo-two-dimensional model of Traineau *et al.*,[13] and the incompressible formula of Taylor.[1] Also, due to the variability that exists among available data, we opt to conduct our own numerical simulations of the porous tube. In the interest of uniformity, we replicate conditions that mimic those implemented by Traineau *et al.*,[13] and subsequently, by Apte and Yang.[19]

Our porous tube is chosen to be 28 cm long with a 1 cm radius and a wall Mach number of 0.0095. We apply a constant mass flux of $13\ \mathrm{kg\cdot m^{-2}\cdot s^{-1}}$ at an injection temperature of 260 K; the fluid is air with a molecular weight of $29\ \mathrm{kg\cdot kmol^{-1}}$, $\gamma = 1.4$, and a dynamic viscosity of $\mu = 1.66\times10^{-5}\ \mathrm{kg\cdot m^{-1}\cdot s^{-1}}$. Unlike Traineau and coworkers, we do not attach a divergent nozzle at the aft end. Our chief concern is with the faithful replication of the geometry used in the mathematical derivation. We recognize that area expansion can expedite convergence, but opt to adhere with Taylor's model, albeit at a small computational expense.

As shown in Fig. 5a, the streamwise variation of p_c is steeper than that of Taylor's or Gany and Aharon's except in the last 15% stretch. It becomes more pronounced with

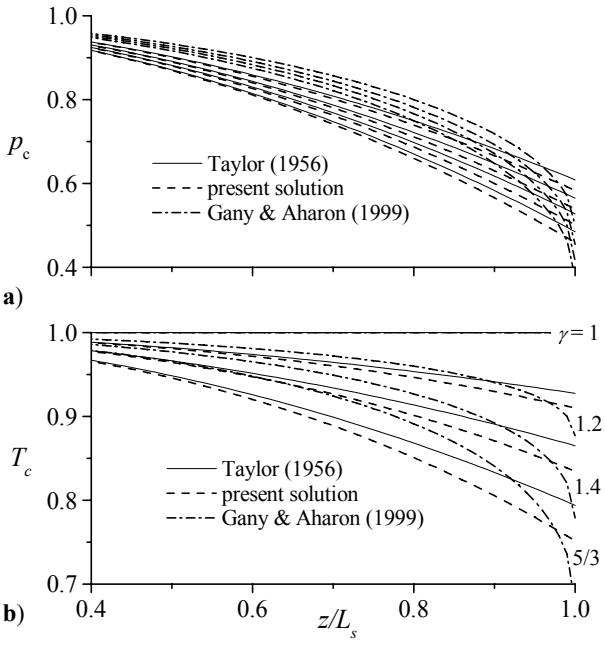

Figure 5. Streamwise evolution of centerline pressures and temperatures using available theories. From outside moving inward, γ= 1, 1.2, 1.4, 1.67.

successive increases in γ. The incremental steepening reflects inevitable departures from the ideal isothermal case for which $\gamma = 1$. The same can be said of the temperature variation in Fig. 5b. In both cases, the one-dimensional model accrues a smaller drop along a major portion of the chamber. It then briskly accelerates in the aft 15% of the length on its way to reclaiming its choke-point value. Its evolution may be traced from

$$p_{1D} = (1+\gamma)^{-1}\left(1+\gamma\sqrt{1-z^2/L_s^2}\right) \quad \text{and} \quad T_{1D} = (1+\gamma)^{1/\gamma-1}\left(1+\gamma\sqrt{1-z^2/L_s^2}\right)^{1-1/\gamma} \tag{75}$$

Note that Gany and Aharon[37] project a critical pressure ratio of $p_s^{(-)} = (1+\gamma)^{-1}$ (at $z = L_s$) although nozzle theory foresees a critical ratio of $p_s^{(+)} = [\frac{1}{2}(\gamma+1)]^{\gamma/(1-\gamma)}$; ours predicts an intermediate quantity. For example, at the sonic point, Eqs. (58) and (62) reduce to

$$p_s = 1-\tfrac{1}{2}\gamma\Gamma^2(1-\tfrac{1}{8}\sigma M_w^2)-\tfrac{1}{24}\gamma\Gamma^4 \quad \text{and} \quad T_s = 1-\tfrac{1}{2}(\gamma-1)\Gamma^2(1-\tfrac{1}{8}\sigma M_w^2)-\tfrac{1}{6}(\gamma-1)\Gamma^4 \tag{76}$$

where Γ may be directly extracted from Eqs. (68), (69), or yet Eq. (67) if a blend with one-dimensional theory is to be entertained. The latter yields the simplest, $\Gamma^2 = 2\gamma^{-1}[1-(\frac{1}{2}\gamma+\frac{1}{2})^{\gamma/(1-\gamma)}]$. The most accurate are

$$\Gamma = \sqrt{\delta\cos\{\tfrac{1}{3}\cos^{-1}[16(14+6\gamma-3\gamma^2-4\gamma^3)/\delta^3]\}-2(\gamma+1)} \quad \text{or} \quad \Gamma = \sqrt{2^{1/3}\lambda-2\gamma-2+2^{2/3}(2\gamma^2+\gamma-1)/\lambda} \tag{77}$$

Both render

$$\Gamma \sim 0.884622-0.177299(\gamma-1)+0.0539119(\gamma-1)^2-0.0180615(\gamma-1)^3 \tag{78}$$

Interestingly, the Taylor series expansion of Γ matches the γ-dependence of the highest order expression for $z_s^{(5)}$ encapsulated by Eq. (70). Furthermore, the M_w^2 term in Eq. (76) may be safely ignored without affecting the three-digit accuracy in the algebraic outcome. For the reader's convenience, a summary of critical pressure and temperature ratios is posted in Table 2.

Table 2. Critical pressure and temperature ratios

γ	$p_s^{(-)}$	p_s	$p_s^{(+)}$	$T_s^{(-)}$	T_s	$T_s^{(+)}$
1.0	0.500	0.583	0.607	1	1	1
1.1	0.476	0.560	0.585	0.935	0.953	0.952
1.2	0.455	0.539	0.564	0.877	0.910	0.909
1.3	0.435	0.519	0.546	0.825	0.871	0.870
1.4	0.417	0.501	0.528	0.779	0.835	0.833
1.5	0.400	0.484	0.512	0.737	0.802	0.800
1.6	0.385	0.469	0.497	0.699	0.771	0.769
5/3	0.375	0.459	0.487	0.675	0.752	0.750

Over the range of γ, our pressure ratio depreciates from 0.583 to 0.459. This constitutes a 16.6 to 22.4% increase in pressure recovery with respect to one-dimensional theory. The increased pressure recovery may be attributed to the absence of viscosity in our model. Had viscosity been accounted for, a larger pressure drop would have been entailed. The one-dimensional model appears to be less vulnerable to friction and attendant irreversibilities: it integrates those away in the process of injecting the flow directly along the axis where viscous damping is the least prominent. Had it been viscous, the current model would have been subject to irreversibilities that consume their share of thermal energy and increase both the temperature and internal energy of the flow. The pressure drop, which is partly a measure of these irreversibilities, would have been larger. The accentuated sensitivity of our axisymmetric representation to viscous losses can therefore explain the larger pressure recoveries observed relative to viscous simulations or one-dimensional approximations.

For example, using $\gamma = 1.4$, our results are compared in Fig. 6a to the CFD pressure curves obtained under two widely accepted turbulent flow models. While the computed k-ω curve nearly coincides with our analytical solution over a significant portion of the chamber, it begins to slightly diverge near the aft end to the extent of closing at 0.400. The Spalart-Allmaras simulation is slightly higher near the headwall but is terminated by the same value. The increased pressure drop compared to ours at 0.501 may be linked to viscous damping. Naturally, the CFD value is nearest to the one-dimensional critical ratio (0.417) proposed by Gany and

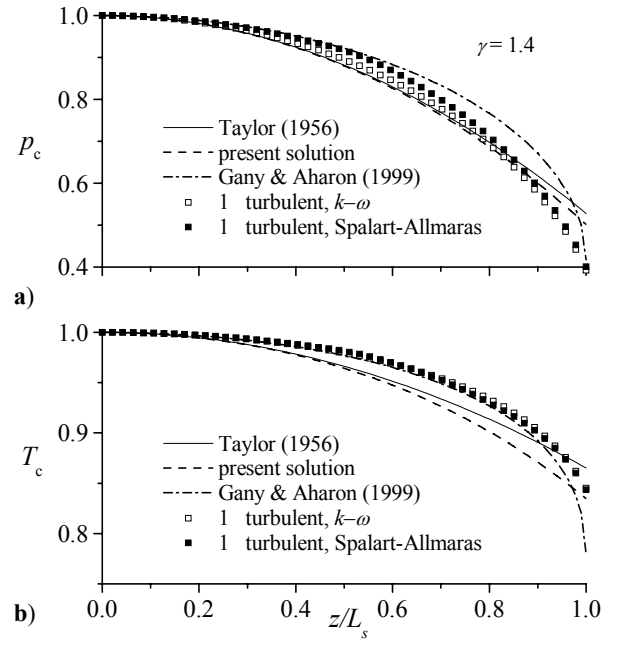

Figure 6. Comparison of theoretical pressures and temperatures to Navier-Stokes computations obtained from two turbulent flow models.

Aharon.[37] Up until the exit section, however, the present solution adequately performs in matching the k-ω curve.

When temperatures are compared in Fig. 6b, an equally interesting behavior is captured. The turbulent-flow computations seem to fall, as predicted, slightly above our theoretical curve; they specifically coincide with the one-dimensional solution over a major portion of the chamber. In contrast to the pressure behavior, a better agreement with our model is seen near the aft end where the numerical curves terminate at 0.845 and 0.843, respectively; this puts them nearest to our theoretical 0.835. A better accord with numerics would thus require the participation of viscosity.

Before leaving this subject, it may be instructive to evaluate the area-averaged quantities as they can provide expeditious estimates. We find,

$$T_m^{(0)} = 1-\tfrac{1}{4}(\gamma-1)M_w^2(2\pi^2z^2+\mathcal{C}+\ln\pi-\mathrm{Ci}\pi) \quad p_m^{(0)} = 1-\tfrac{1}{4}\gamma M_w^2(2\pi^2z^2+\mathcal{C}+\ln\pi-\mathrm{Ci}\pi) \text{ (Taylor's)} \tag{79}$$

and

$$\begin{cases} p_m = p_m^{(0)} - \frac{1}{384}\gamma\pi^2M_w^4[\pi^2(16z^4+12z^2+5)-3\sigma(8z^2+1)] \\ T_m = T_m^{(0)} - \frac{1}{384}(\gamma-1)M_w^4\{48+\pi^4(64z^4+12z^2+5)-3\pi^3\alpha(8z^2+1) \\ \qquad\qquad +6\pi^2[\beta+8z^2(\beta+\mathcal{C}-\mathrm{Ci}\pi+\ln\pi)]-12\pi(\alpha-4\mathrm{Si}\pi)\} \end{cases} \tag{80}$$

Although not shown on the graphs, p_m and T_m vary in concert with their counterparts taken along the axis. This reaffirms the frail pressure and temperature gradients in the radial direction. It also justifies the appropriateness of earlier comparisons between centerline properties and area-averaged one-dimensional projections.

H. Characteristic Effects of Compressibility

Having established the importance of L_s as a geometric scaling parameter, we can use it to delineate the zone of validity for the subsonic region. We show this in Fig. 7 at four representative values of γ. The minute shifts in the sonic curves reflect the weak sensitivity of the solution to the ratio of specific heats. This reinforces the notion of recouping a nearly frozen state after rescaling with respect to L_s.

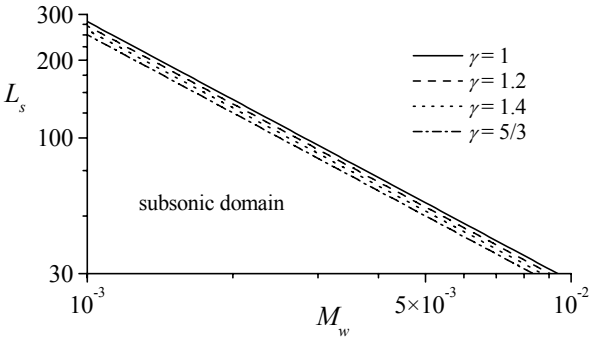

Figure 7. Sonic distance versus wall Mach number.

Considering a chamber of length L_s as our baseline case, the spatial evolution of the velocity field across the entire domain may be captured independently of the Mach number. This is illustrated in Fig. 8 where both streamwise and radial components are plotted in the upper and lower parts of the graph, respectively. These represent scaled-down versions that preserve the relative proportions of actual magnitudes. The former plot is repeated in the middle part where it is magnified for better

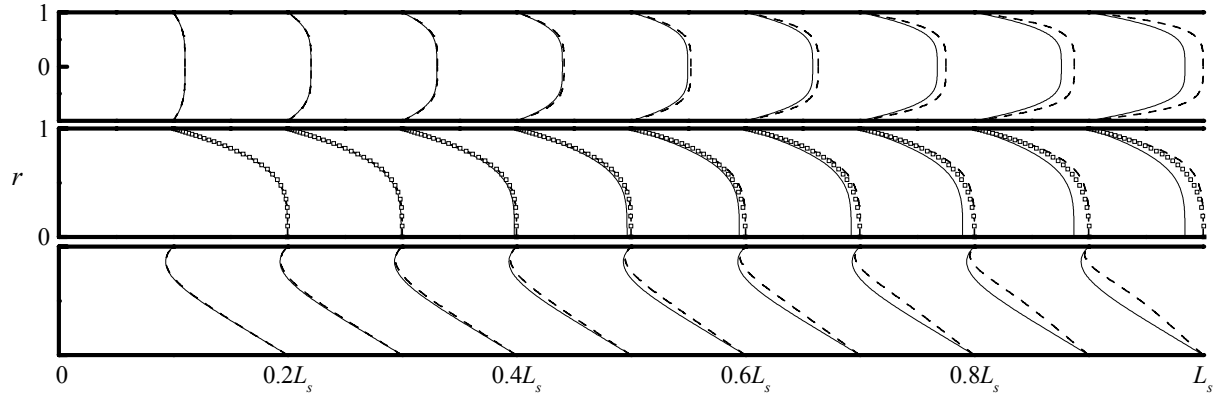

Figure 8. Spatial evolution of axial and radial velocity profiles up to the sonic point. Although we use a wall Mach number of 0.01 and L_s = 28, relative proportions are universal. The inset rescales the axial velocity by its centerline value and compares it to CFD data (hollow squares for the k-ω model). The gradual flattening of the compressible profile past $L_s/2$ is corroborated by both theory and experiment.

clarity (using the local centerline speed) and compared to CFD predictions. These are shown at 9 equally-spaced axial stations corresponding to 0.1, 0.2, 0.3, . . . , and 0.9 L_s. Although we use operating parameters that co-tail our computational model, we emphasize the geometric similarity that renders this plot universal. Its response to changing γ is so minor that it may be ignored. This is verified by modifying the Mach number from 0.0001 to 0.01 with no distinct influence on the solution. Changing γ from 1 to 5/3 has some influence, but it is too small to deserve particular attention.

As expected, these profiles bear a striking resemblance to the numerical results and to both laboratory and computational experiments obtained by Traineau, Hervat and Kuentzmann,[13] Balakrishnan, Liñan and Williams,[29] Apte and Yang,[18,19] and others. Specifically, we note that the streamwise velocity becomes much fuller than Taylor's sinusoidal profile as choking is approached. This is accompanied by the classic linearization of the radial velocity. The evolution into a blunter, turbulent-like, or pseudo-one-dimensional plug flow is conformant to both theory and experiment. It faithfully captures the increased gradients at the sidewall and these can have important implications in mean-flow related analyses. To the author's knowledge, this represents the first explicit analogue of Taylor's compressible flow that exhibits the correct steepening behavior. Its agreement with CFD predictions is remarkable despite the presence of small viscosity in the numerical simulation.

In order to quantify the steepening effect and magnification caused by compressibility, theoretical and CFD profiles are overlaid in Fig. 9. In Fig. 9a, the streamwise velocity, normalized by $\pi z M_w$, is shown at four evenly spaced distances from the sonic point. Because the leading order sinusoidal profile varies between 0 and 1, it can be conveniently adopted as a benchmark. The amplification of the streamwise velocity can thus be inferred relative to Taylor's model. We note that, below $0.4L_s$, the compressible solution and Taylor's overlap (the discrepancy between them being less than 2%). This justifies the use of Taylor's in chambers whose actual length is roughly $L \le 0.4L_s$. The precise cutoff point is always a matter of conjecture but we shall attempt to define it based on the relative error with respect to Taylor's. So first, this relative error must be characterized. As shown in Fig. 9b, the maximum difference between the axial velocities, which appears at the centerline, can be evaluated. Being commensurate with the local impact of fluid compression, the ratio $\vartheta_c = u_z(0,z)/u_z^{(0)}(0,z) = u_z(0,z)/(\pi z M_w)$ becomes a direct measure of relative amplification. For example, the theoretical amplification at $z = L_s$ can be determined to be 1.112 versus a computed value of 1.133; the CFD limit is converged upon by each of the turbulent

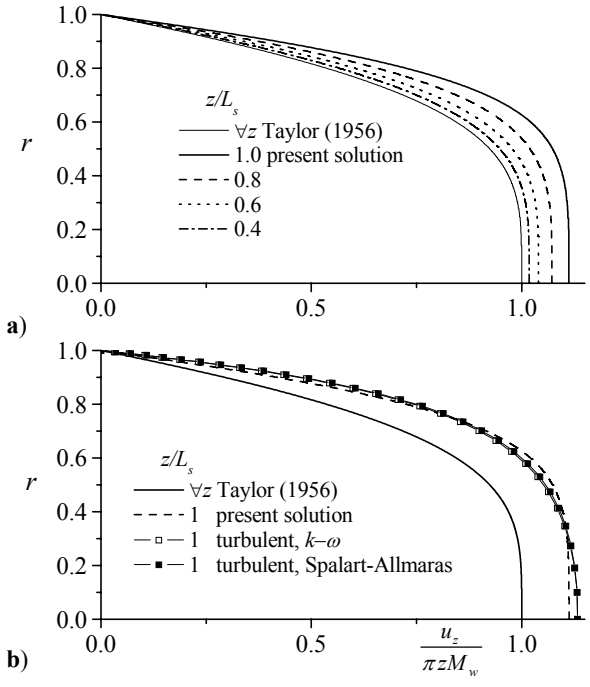

Figure 9. Gradual steepening of the streamwise velocity as choking is approached. Computational curves are shown in b) at the critical location. The normalized Taylor profile is axially invariant.

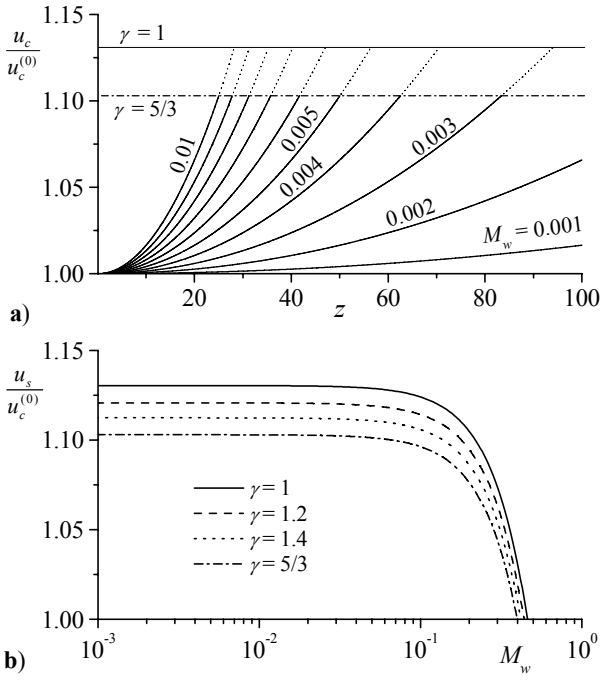

Figure 10. We show in a) the effect of varying M_w on the compressible centerline velocity ratio as choking is axially approached. The maximum velocity ratio at the sonic point is shown in part b).

models. Despite selecting the (most) critical location, a nearly perfect match with the turbulent profiles is realized in both fullness and extent. The turbulent simulations are performed using two standard schemes, namely, the *k-ω* and Spalart-Allmaras.[40] These yield such similar distributions that their differences are graphically imperceptible. The concurrence of the analytical solution with turbulent simulations is gratifying, especially that the model is often applied to problems involving large crossflow Reynolds numbers. The concurrence with turbulent predictions is not an artifact but rather an attribute of inviscid flows.

Overall, the amplification at a radial position can be measured from the ratio of velocities, $\vartheta(r,z) \equiv u_z / u_z^{(0)}$. At any cross section, the maximum local ratio occurs along the centerline where $\vartheta_c(z) \equiv u_c / u_c^{(0)}$. The smallest increase in ϑ_c can have an appreciable impact on core flow ingredients, including the growth rate of disturbances. As recently shown in a compressible flow simulation of a model rocket motor, a roughly 10% increase in centerline speed (caused by density variations) can lead to a 70% overshoot in the growth of oscillatory wave amplitudes at a streamwise location of 40 (cf. pp. 61-65, Venugopal[34]). The evolution of ϑ_c with distance from the headwall is illustrated in Fig. 10a over a wide range of operating parameters and up to the sonic point. The latter occurs sooner at higher γ. Since the critical length depends on the gas compression ratio, dotted lines are used in the buffer region that is bracketed by the upper and lower bounds for γ. As M_w is lowered, it appears that, for the chosen range of Mach numbers, the relative amplification ratio increases to a pure constant at fixed γ. This observation prompts us to define the maximum overall velocity amplification, $\vartheta_s = u_s / u_c^{(0)}$, based on $u_s = u_c(L_s)$. In Fig. 10b, a plot of ϑ_s confirms our hypothesis. We find that the sonic amplification ratio does indeed asymptote to a constant value in the practical range of Mach numbers. The asymptotic limit varies between 1.130 for $\gamma = 1$ to 1.103 for $\gamma = 5/3$. Analytically, the corresponding magnification may be obtained from Eq. (63) such that

$$\vartheta_c = 1 + \tfrac{1}{6}\pi^2 M_w^2 z^2 - \tfrac{1}{16}\sigma M_w^2 \quad \text{or} \quad \tilde{\vartheta}_c = 1 + \tfrac{1}{6}\pi^2 M_w^2 z^2 - \tfrac{1}{2} M_w^2 \tag{81}$$

By insertion of Γ, we collect $\vartheta_c = 1 + \tfrac{1}{6}\Gamma^2 X^2 - \tfrac{1}{16}\sigma M_w^2 \sim 1 + \tfrac{1}{6}\Gamma^2 X^2$. The asymptotic amplification for $X = 1$ may be readily estimated from

$$\vartheta_s^* \sim 1 + \tfrac{1}{6}\Gamma^2 \sim 1.13043 - 0.0522808(\gamma - 1) + 0.0211364(\gamma - 1)^2 - 0.00851203(\gamma - 1)^3$$

In applications that feature $M_w > 0.02$, an additional correction is required, specifically,

$$\vartheta_s = \vartheta_s^* - M_w^2[0.641014 + 0.0487504(\gamma - 1) - 0.0186428(\gamma - 1)^2] \tag{82}$$

These quantities enable us to directly measure the propensity of fluid compression and its bearing on the mean flow.

I. Extension to Solid and Hybrid Rockets

One may wonder under what circumstances will density variations become important in SRMs. The present study can help to answer this question given a desired level of precision set by the designer. Suppose that an error that exceeds $\varepsilon = 4\%$ over more than $x = \tfrac{1}{4}$ of the chamber length is deemed unacceptable. Our solution enables us to calculate the distance to reach such degree of disparity with respect to Taylor's equation. This is met when $\vartheta_c = 1 + \varepsilon$, or, to good approximation, at

$$z_\varepsilon = \frac{1}{\pi M_w}\sqrt{6\varepsilon} \tag{83}$$

If $z_\varepsilon a < (1 - x)L_0$, then volumetric expansions must be accounted for. By applying this formula in reverse to a chamber with a relatively large aspect ratio, say $L = 50$, we find the (minimum) cutoff Mach number M_w^* that must be surpassed for this condition to hold. This is

$$M_w^* = \frac{1}{\pi(1 - x)L}\sqrt{6\varepsilon} \simeq 0.0042 \tag{84}$$

Thus if this motor has $M_w > M_w^*$, a 4% error will affect more than its aft quarter length. Otherwise, it may be safely treated using Taylor's formula. Considering that many SRMs operate under $M_w = 0.0042$ and have lengths that are shorter than $L = 50$, the suitability of Taylor's model remains unchallenged in those particular instances. The current solution becomes necessary, however, in applications that exhibit accentuated sensitivity to the mean flow. Examples include the full-scale numerical simulations conducted by CSAR, the treatment of the Stokes acoustic layer with sidewall injection (cf. Wasistho, Balachandar, and Moser[28]), the investigation of instability (cf. Venugopal, Najjar and Moser[41]), and the analysis of the exothermic boundary layer (cf. Balakrishnan, Liñan and Williams[29]). Surely, when precision is required to mitigate unwanted deviations, the present solution may be resorted to. Overall, it increases our arsenal of physical approximations for the treatment of high speed compressible flow.

If the interest is shifted to the modeling of hybrid rockets, one may repeat the analysis presented here using a nonzero inlet velocity at the headwall. One can use, for example, the similarity-conforming cosine shape proposed by Majdalani and Vyas;[42] this classic profile dating back to Berman (1953)[8] was presented in the context of providing an inviscid, outer approximation for the steady streamtube motion in hybrid rockets. Although it does not enforce an inlet condition on u_r, it remains quasi viscous as it fully observes the no slip condition along the sidewall.

For implementation, the fourth boundary condition in Eq. (9) must be properly altered; as before, we write $u_z(r,0) = M_0 \cos(\frac{1}{2}\pi r^2)$, $M_0 \equiv U_0 / a_0$. Note that only the streamwise velocity is constrained at the headwall. No condition is imposed on the radial inflow component. The notion of an open boundary at $z = 0$ is suitable in hybrid rocket applications where the injection at the headwall is not necessarily orthonormal to the surface. Some injectors are deliberately designed with a nonzero angle of attack.

As meticulously derived in a previous study, the solution connected with a sinusoidal headwall injection can be recovered by shifting the origin of Taylor's model to a hypothetical station located (upstream of the headwall) at a distance of $z = -u_h$, where $u_h = u_0 / \pi$. A simple translation of the axis will hence enable us to modify the solution appropriately. One can write, for example,

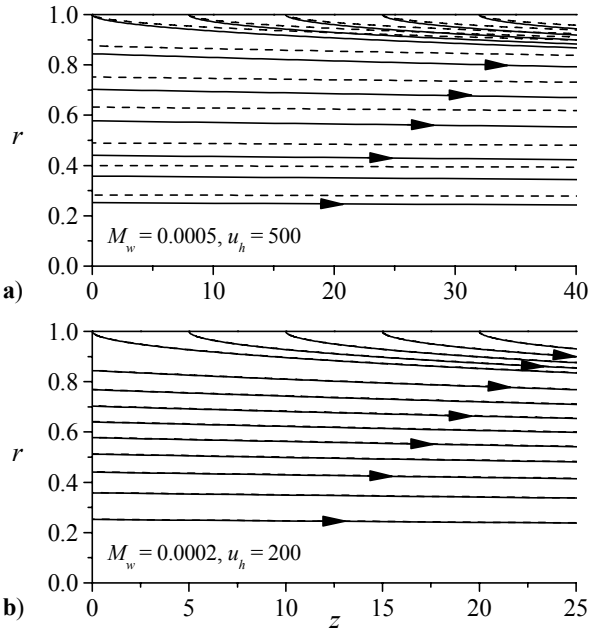

Figure 11. Streamlines corresponding to a hybrid rocket model with sinusoidal headwall injection. While conditions in a) are susceptible to fluid compression, the flow in b) is nearly incompressible. Here we use $\gamma = 1.2$. This model tends to approximate the characteristic streamtube motion reported in hybrid core flow.

$$\tilde{\psi} = M_w \psi^{(0)} \left(1 - \tfrac{1}{4} M_w^2 \left\{ \pi^2 (z+u_h)^2 \left[1 + \tfrac{1}{3} \cos(\pi r^2) \right] + 2 \right\} \right) \tag{85}$$

where $\psi^{(0)} = (z+u_h)\sin\eta$ represents the extended version of Taylor's formula with sinusoidal headwall injection.[42] The foregoing expressions can be modified straightforwardly by replacing the streamwise coordinate by $Z = z + u_h$. At the outset, the critical length must be rectified by subtracting from it the headwall effect. The new effective distance to the sonic point becomes $L_h = L_s - u_h$. This correction has a large bearing on the hybrid model because it suggests that compressibility may be important despite a small M_w so long as u_h is sufficiently large. All depends on M_w and the relative length of the hybrid chamber with respect to L_h. The criterion given by Eq. (84) translates into

$$M_w^* = \frac{1}{\pi[(1-x)L + u_h]} \sqrt{6\varepsilon} \quad \text{(including headwall injection)} \tag{86}$$

The effect of fluid compression in hybrids is illustrated in Fig. 11 at two sets of parameters. These correspond to circumstances under which the cutoff M_w^* is a) 0.0003 and b) 0.0007. Since the wall Mach number in Fig. 11a exceeds 0.0003, compressibility effects are seen to permeate the chamber. The converse may be said of Fig. 11b where no deviations from Taylor's formula are visible. Equation (86) provides a simple but helpful tool for judging whether a compressible or incompressible solution is required in the modeling of solid and hybrid rockets. It must be noted that, in recent years, hybrid rocket development has continued to evolve. The latest data suggests typical aspect ratios ranging from 20 to 80 and headwall Mach numbers reaching 0.3-0.5.[43] Using a hybrid wall Mach number of $M_w \simeq 0.0003$, one calculates the headwall injection constant to be upward of 1,000. Under such high speed conditions, compressibility becomes quintessential.

J. Reconstruction and Critique of Flandro's Compressible Solution

Flandro must be credited for having been first to explore this problem in a formal quasi-two-dimensional setting.[44] This was carried out in the context of analyzing the effects of high speed mean flows on the unsteady wave motion in elongated SRMs. In the process, a similar methodology to the one presented here was implemented.

In fact, one may reconstruct Flandro's solution directly from ours. This can be accomplished in three easy steps. From Eq. (32) one may ignore all but the leading order dependence on the radial coordinate to the extent of putting

$$q(\eta,z)=\tfrac{1}{8}\pi\eta z\left\{-4+\sin(2\eta)/\eta-4\cos(2\eta)+8\pi\eta z^2-(8/\pi^3)\eta G(z\sin\eta)/(z\sin\eta)\right\}\simeq-\tfrac{1}{2}\pi\eta z \tag{87}$$

Moreover, by letting $F(\eta,z)\simeq F(z)$ be a sole function of the streamwise coordinate, the transformed vorticity equation given by Eq. (31) may be leveled to

$$\underbrace{\eta^2\frac{\partial^2 F}{\partial\eta^2}+2\eta^2\cot\eta\frac{\partial F}{\partial\eta}}_{0}+\frac{\eta}{2\pi}\frac{\partial^2 F}{\partial z^2}\simeq\frac{\eta}{2\pi}\frac{\mathrm{d}^2 F}{\mathrm{d}z^2}=-\tfrac{1}{2}\pi\eta z\quad\text{or}\quad\frac{\mathrm{d}^2 F}{\mathrm{d}z^2}=-\pi^2 z \tag{88}$$

Rarely could integration be missed at this point. One finds

$$F=-\tfrac{1}{6}\pi^2 z^3+K_1 z+K_2 \tag{89}$$

Recalling that $\psi^{(1)}=F\sin\eta$, conditions (a) and (d) in Eq. (42) are immediately satisfied. To secure the no slip and radial inflow boundary conditions, Eq. (45) may be applied. One collects $K_1=-\frac{1}{2}$ and $K_2=0$. The first order solution $\psi_F^{(1)}$ obtained under these auspices is expressible by

$$\psi_F^{(1)}=-\tfrac{1}{6}(\pi^2 z^2+3)z\sin\eta \tag{90}$$

This is precisely the formula obtained by Flandro.[44]

Despite its ability to satisfy the main auxiliary conditions, Eq. (90) does not exhibit the correct steepening behavior. Its centerline velocity overshoots the correct value at choking by twice the actual amount. Upon closer look, these discrepancies may be attributed to several underlying limitations. The first concerns the assumption that $\Omega^{(1)}=\pi^2 r\psi^{(1)}$ must mirror the leading order behavior. This conjecture suppresses the correction $\Omega_c^{(1)}$ which is needed to satisfy the first order vorticity transport equation. In the present analysis, we prove $\Omega_c^{(1)}$ to be vital lest the vorticity transport equation $\nabla\times\boldsymbol{u}^{(0)}\times\boldsymbol{\Omega}^{(1)}+\nabla\times\boldsymbol{u}^{(1)}\times\boldsymbol{\Omega}^{(0)}=0$ is violated. Additionally, we view the subsequent dismissals in the vorticity equation preventable. As shown earlier, the complete vorticity equation can be solved (exactly) using a formal mathematical strategy. By discounting the radial dependence in Eq. (30), a large residual error is incurred to the extent that neither the vorticity nor the momentum equations are satisfied. This renders Eq. (90) unphysical. The growing residual error in the vorticity equation is illustrated in Fig. 12 where it is compared to its counterpart in the compact solution $\tilde{\psi}^{(1)}$ (here we plot their ratio). The discontinuity at r = 0.81734 is due to the vanishing error in $\tilde{\psi}^{(1)}$. Clearly, the error entailed in truncating the vorticity equation is not negligible. To reconcile with our asymptotic solution, Eq. (90) must be augmented by a key correction, specifically,

$$\tilde{\psi}^{(1)}=\psi_F^{(1)}-\tfrac{1}{6}\pi^2 z^3\cos^2\eta\sin\eta \tag{91}$$

Equation (90) is not without merit. It remains the first analytical expression to have been advanced in the literature and a further testimony to Flandro's legacy that has stretched from significant contributions in orbital mechanics (e.g., his discovery of the Voyager Grand Tour Mission trajectory) to outstanding achievements in rocket internal flow modeling.

V. Conclusions

In this study, the compressible flow analogue to the Taylor-Culick problem has been solved analytically and presented in two closed forms: one exact, satisfying all first principles, and one approximate, retaining the essence of the solution. These key findings lead to a formidable leap in our physical understanding of compressible flow behavior in multidimensional settings. In propulsion-rooted applications, they permit the re-evaluation of many ballistic performance measures which, so far, have been mostly confined to one-dimensional platforms.

The most significant result is perhaps the advent of a compact analytical expression for the streamwise and wall-normal velocity profiles which, unlike other models, can be calculated easily. It is gratifying that our solution can reproduce up to the sonic point the fullness and extent of Navier-Stokes profiles computed using two reliable models of turbulence. The second significant result is the discovery of the choking length as the appropriate scale leading to nearly frozen behavior irrespective of the wall

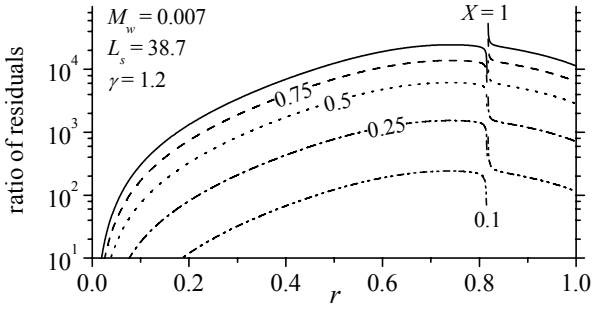

Figure 12. Residual error in Eq. (90) with respect to $\tilde{\psi}^{(1)}$.

Mach number; this has enabled us to recast the solution in a more portable, parametric-free form. In the wake of this generalization, simple design criteria that quantify the relative weight of gas compression have been deduced and shown to realistically project actual behavior. Due to the particular role that it plays, the sonic length has been derived and presented using several approximations of increasing precision. The amplification of the centerline velocity, a key parameter in core flow analysis, has also been characterized and tacitly secured.

By circumventing the need to compute the mean flow at each point and set of operating variables, our compact solutions greatly facilitate parametric trade analyses. This includes the investigation of hydrodynamic instability of solid and hybrid rockets. The fact that our streamlines are steepened at higher Mach numbers and fixed length lends support to Griffond's and Venugopal's recent hypotheses; these ascribe the heightened stability sensitivity to steeper streamline curvatures.[34,38] In light of this consensus regarding the destabilizing role of fluid dilatation, further exploratory studies may be warranted.

The small differences we found in pressure and temperature estimations have been linked to the absence of viscosity in our model. This motivates the quest for a two-pronged viscous and compressible mean flow solution that follows familiar lines.[20] Incorporating friction may be useful in modeling hybrid rocket core flows in which the wall Reynolds number is small in comparison to SRMs. The use of a refined compressible model is hoped to improve our strategy in analyzing unsteady vortico-acoustic wave propagation and stability in porous enclosures. Repeating the analysis with constant mass-flux surface conditions may also provide a more appropriate model vis-à-vis some existing experimental and numerical simulations. Finally, having demonstrated the viability of the present methodology, the work may be extended to other geometric settings. In short, a plethora of research topics are now open to future investigation.

Acknowledgments

This work is sponsored by the CAREER Program of the National Science Foundation through Grant No. CMS-0353518, Program Manager, Dr. Masayoshi Tomizuka. The author wishes to thank: M. J. Chiaverini, Chair, AIAA Technical Committee on Hybrids, for helpful discussions; B. A. Maicke, graduate student at the University of Tennessee Space Institute, for providing the CFD results; P. Venugopal, Research Engineer, Philips Medical Systems, University of California at Los Angeles, for valuable comments; and A. B. Vyas, Visiting Researcher at the Department of Mathematical Sciences, University of Delaware, for verifying the higher order pressures and temperatures.

References

[1]Taylor, G. I., "Fluid Flow in Regions Bounded by Porous Surfaces," *Proceedings of the Royal Society, London, Series A,* Vol. 234, No. 1199, 1956, pp. 456-475.

[2]Yuan, S. W., "Further Investigation of Laminar Flow in Channels with Porous Walls," *Journal of Applied Physics,* Vol. 27, No. 3, 1956, pp. 267-269.

[3]Yuan, S. W., and Finkelstein, A. B., "Laminar Pipe Flow with Injection and Suction through a Porous Wall," *Transactions of the American Society of Mechanical Engineers: Journal of Applied Mechanics, Series E,* Vol. 78, No. 3, 1956, pp. 719-724.

[4]Wageman, W. E., and Guevara, F. A., "Fluid Flow through a Porous Channel," *The Physics of Fluids,* Vol. 3, No. 6, 1960, pp. 878-881.

[5]Terrill, R. M., "Laminar Flow in a Uniformly Porous Channel," *The Aeronautical Quarterly,* Vol. 15, 1964, pp. 299-310.

[6]Terrill, R. M., "Laminar Flow in a Uniformly Porous Channel with Large Injection," *The Aeronautical Quarterly,* Vol. 16, 1965, pp. 323-332.

[7]Culick, F. E. C., "Rotational Axisymmetric Mean Flow and Damping of Acoustic Waves in a Solid Propellant Rocket," *AIAA Journal,* Vol. 4, No. 8, 1966, pp. 1462-1464.

[8]Berman, A. S., "Laminar Flow in Channels with Porous Walls," *Journal of Applied Physics,* Vol. 24, No. 9, 1953, pp. 1232-1235.

[9]Yuan, S. W., "Cooling by Protective Fluid Films," *Turbulent Flows and Heat Transfer,* Section G, Vol. V, edited by C. C. Lin, Princeton University Press, Princeton, New Jersey, 1959.

[10]Peng, Y., and Yuan, S. W., "Laminar Pipe Flow with Mass Transfer Cooling," *Journal of Heat Transfer,* Vol. 87, No. 2, 1965, pp. 252-258.

[11]Yamada, K., Goto, M., and Ishikawa, N., "Simulative Study of the Erosive Burning of Solid Rocket Motors," *AIAA Journal,* Vol. 14, No. 9, 1976, pp. 1170-1176.

[12]Dunlap, R., Willoughby, P. G., and Hermsen, R. W., "Flowfield in the Combustion Chamber of a Solid Propellant Rocket Motor," *AIAA Journal,* Vol. 12, No. 10, 1974, pp. 1440-1445.

[13]Traineau, J. C., Hervat, P., and Kuentzmann, P., "Cold-Flow Simulation of a Two-Dimensional Nozzleless Solid-Rocket Motor," AIAA Paper 86-1447, July 1986.

[14]Beddini, R. A., "Injection-Induced Flows in Porous-Walled Ducts," *AIAA Journal,* Vol. 24, No. 11, 1986, pp. 1766-1773.

[15]Baum, J. D., Levine, J. N., and Lovine, R. L., "Pulsed Instabilities in Rocket Motors: A Comparison between Predictions and Experiments," *Journal of Propulsion and Power,* Vol. 4, No. 4, 1988, pp. 308-316.

[16]Sabnis, J. S., Gibeling, H. J., and McDonald, H., "Navier-Stokes Analysis of Solid Propellant Rocket Motor Internal Flows," *Journal of Propulsion and Power,* Vol. 5, No. 6, 1989, pp. 657-664.

[17]Liou, T.-M., and Lien, W.-Y., "Numerical Simulations of Injection-Driven Flows in a Two-Dimensional Nozzleless Solid-Rocket Motor," *Journal of Propulsion and Power,* Vol. 11, No. 4, 1995, pp. 600-606.

[18]Apte, S., and Yang, V., "Effect of Acoustic Oscillation on Flow Development in a Simulated Nozzleless Rocket Motor," *Solid Propellant Chemistry, Combustion, and Motor Interior Ballistics*, Vol. 185, edited by V. Yang, T. B. Brill, and W.-Z. Ren, AIAA Progress in Astronautics and Aeronautics, Washington, DC, 2000, pp. 791-822.

[19]Apte, S., and Yang, V., "Unsteady Flow Evolution in a Porous Chamber with Surface Mass Injection. Part I: Free Oscillation," *AIAA Journal,* Vol. 39, No. 8, 2001, pp. 1577-1586.

[20]Majdalani, J., Vyas, A. B., and Flandro, G. A., "Higher Mean-Flow Approximation for a Solid Rocket Motor with Radially Regressing Walls," *AIAA Journal,* Vol. 40, No. 9, 2002, pp. 1780-1788.

[21]King, M. K., "Consideration of Two-Dimensional Flow Effects on Nozzleless Rocket Performance," *Journal of Propulsion and Power,* Vol. 3, No. 3, 1987, pp. 194-195.

[22]Chu, W.-W., Yang, V., and Majdalani, J., "Premixed Flame Response to Acoustic Waves in a Porous-Walled Chamber with Surface Mass Injection," *Combustion and Flame,* Vol. 133, No. 6129, 2003, pp. 359-370.

[23]Vuillot, F., "Vortex-Shedding Phenomena in Solid Rocket Motors," *Journal of Propulsion and Power,* Vol. 11, No. 4, 1995, pp. 626-639.

[24]Majdalani, J., "Physicality of Core Flow Models in Rocket Motors," *Journal of Propulsion and Power,* Vol. 19, No. 1, 2003, pp. 156-159.

[25]Varapaev, V. N., and Yagodkin, V. I., "Flow Stability in a Channel with Porous Walls," *Fluid Dynamics (Izvestiya Akademii Nauk SSSR, Meckanika Zhidkosti i Gaza),* Vol. 4, No. 5, 1969, pp. 91-95.

[26]Griffond, J., Casalis, G., and Pineau, J.-P., "Spatial Instability of Flow in a Semiinfinite Cylinder with Fluid Injection through Its Porous Walls," *European Journal of Mechanics B/Fluids,* Vol. 19, No. 1, 2000, pp. 69-87.

[27]Féraille, T., and Casalis, G., "Channel Flow Induced by Wall Injection of Fluid and Particles," *The Physics of Fluids,* Vol. 15, No. 2, 2003, pp. 348-360.

[28]Wasistho, B., Balachandar, S., and Moser, R. D., "Compressible Wall-Injection Flows in Laminar, Transitional, and Turbulent Regimes: Numerical Prediction," *Journal of Spacecraft and Rockets,* Vol. 41, No. 6, 2004, pp. 915-924.

[29]Balakrishnan, G., Liñan, A., and Williams, F. A., "Rotational Inviscid Flow in Laterally Burning Solid Propellant Rocket Motors," *Journal of Propulsion and Power,* Vol. 8, No. 6, 1992, pp. 1167-1176.

[30]Majdalani, J., and Flandro, G. A., "The Oscillatory Pipe Flow with Arbitrary Wall Injection," *Proceedings of the Royal Society, Series A,* Vol. 458, No. 2022, 2002, pp. 1621-1651.

[31]Majdalani, J., and Roh, T. S., "The Oscillatory Channel Flow with Large Wall Injection," *Proceedings of the Royal Society, Series A,* Vol. 456, No. 1999, 2000, pp. 1625-1657.

[32]Majdalani, J., "The Oscillatory Channel Flow with Arbitrary Wall Injection," *Journal of Applied Mathematics and Physics,* Vol. 52, No. 1, 2001, pp. 33-61.

[33]Balakrishnan, G., Liñan, A., and Williams, F. A., "Compressible Effects in Thin Channels with Injection," *AIAA Journal,* Vol. 29, No. 12, 1991, pp. 2149-2154.

[34]Venugopal, P., "Direct Numerical Simulation of Turbulence in a Model Solid Rocket Motor," Ph.D. Dissertation, University of Illinois at Urbana-Champaign, 2003.

[35]Flandro, G. A., "Effects of Vorticity on Rocket Combustion Stability," *Journal of Propulsion and Power,* Vol. 11, No. 4, 1995, pp. 607-625.

[36]Flandro, G. A., and Majdalani, J., "Aeroacoustic Instability in Rockets," *AIAA Journal,* Vol. 41, No. 3, 2003, pp. 485-497.

[37]Gany, A., and Aharon, I., "Internal Ballistics Considerations of Nozzleless Rocket Motors," *Journal of Propulsion and Power,* Vol. 15, No. 6, 1999, pp. 866-873.

[38]Griffond, J., "Receptivity and Aeroacoustic Resonance in Channels with Blowing Walls," *The Physics of Fluids,* Vol. 14, No. 11, 2002, pp. 3946-3962.

[39]Dunlap, R., Blackner, A. M., Waugh, R. C., Brown, R. S., and Willoughby, P. G., "Internal Flow Field Studies in a Simulated Cylindrical Port Rocket Chamber," *Journal of Propulsion and Power,* Vol. 6, No. 6, 1990, pp. 690-704.

[40]Maicke, B. A., Private Communication, 2005.

[41]Venugopal, P., Najjar, F. M., and Moser, R. D., "Numerical Simulations of Model Solid Rocket Motor Flows," AIAA Paper 2001-3950, July 2001.

[42]Majdalani, J., and Vyas, A. B., "Inviscid Models of the Classic Hybrid Rocket," AIAA Paper 2004-3474, July 2004.

[43]Chiaverini, M. J., Chair, AIAA Technical Committee on Hybrids, Private Communication, 2005.

[44]Flandro, G. A., "Stability Prediction for Solid Propellant Rocket Motors with High-Speed Mean Flow," Air Force Rocket Propulsion Laboratory, Final Technical Rept. AFRPL-TR-79-98, Edwards AFB, CA, August 1980.